

**Final report for MSc Project**

---

**Mechanisms governing High Frequency AC nerve block –  
A Modelling and Simulation study**

---

**Theo Bacon Gardner**

Supervisor(s): Dr Konstantin Nikolic

Submitted in partial fulfilment of the requirements for the award of MSc in Biomedical  
Engineering from Imperial College London

September 2018

Word count: 7056

## **Abstract**

High-frequency (HFAC) nerve block has been widely studied in recent years as a potential neuromodulation therapy, however the mechanisms underpinning the technique are still not fully understood at a biophysical level. In this study, three computational nerve models were constructed with the aim of gaining insight into these mechanisms and to assess their accuracy in replicating experimental findings of the phenomenon. Models included a lumped circuit cable model of an unmyelinated axon based on Hodgkin-Huxley equations, a double-cable model of a myelinated mammalian axon, and a cable model of an unmyelinated C-fibre axon. Results found that the stimulation intensity threshold required for block increased linearly with increasing frequency across all models, as well as a decrease in threshold with increasing fibre diameter, and a logarithmic increase in threshold with increasing inter-electrode distance (IED). Square waveform stimulation was also shown to exhibit a lower block threshold in comparison to sinusoidal stimulation. For both the unmyelinated Hodgkin-Huxley axon model and the myelinated mammalian axon model, the specific mechanisms responsible for block were found to be dependent on a steady state of tonic depolarisation induced by the HFAC stimulation. Interestingly for the C-fibre model however, mechanisms for block were dependent on a steady state of tonic hyperpolarisation. It is believed that this has yet to be shown in any published computational or experimental studies on HFAC nerve block to date. This study hopes to provide knowledge that can help improve existing nerve models for HFAC block, thus accelerating its development as a clinically and commercially available treatment.

# Contents

1.	Introduction .....	4
1.1	Modelling of Peripheral Nerve Fibres for Conduction Block .....	4
1.2	Characteristics of HFAC nerve block .....	5
2.	Methods .....	7
2.1	H-H Unmyelinated Axon model.....	8
2.2	MRG Axon Model.....	9
2.3	C-fibre Axon Model with Ion Diffusion.....	11
2.4	Simulation setup .....	12
3.	Results .....	13
3.1	Demonstration of block .....	13
3.2	Block threshold curves .....	14
3.3	Mechanisms for block .....	15
3.3.1	Hodgkin-Huxley model.....	15
3.3.2	MRG model.....	19
3.3.3	C-fibre model .....	20
4.	Discussion .....	23
	Globally investigated variables .....	23
	Onset response.....	24
	Biophysical mechanisms .....	24
	Analysis of C-fibre model .....	25
	Improvements .....	25
5.	Conclusion.....	26
	References .....	27
	Appendices .....	29
	Appendix A – H-H axon model .....	29
	Appendix B – MRG axon model.....	30
	Appendix C – C-fibre axon model .....	34

# 1. Introduction

Many debilitating medical conditions are characterised by overactive or undesirable peripheral nerve activity, resulting in pain, muscle spasms and other unwanted sensations. Such conditions include spinal cord injuries [1], multiple sclerosis [2], and cardiac, inflammatory and metabolic diseases such as rheumatoid arthritis that can lead to hyperactivity in some autonomic circuits [3],[4]. Therefore, in clinical applications the ability to produce a selective and reversible conduction block of peripheral nerve fibres would be of much value. High-frequency AC (HFAC) nerve block provides a potential candidate for such a technique, having become widely studied in the last decade as a neuromodulation therapy due to its appeal over alternatives. Existing treatments for the blocking of nerve fibres are mostly surgical or pharmacological and have significant disadvantages such as non-specificity, side-effects, nerve destruction and low success rates [5], whereas if utilised effectively HFAC nerve block has shown to produce a rapid and quickly reversible inhibition of action potential propagation that can be focussed locally and without any apparent damage to the nerve [5],[6]. Despite this, refinement of the technique has been slow due to a lack in understanding of the specific biophysical mechanisms underpinning HFAC block. Computational models, as well as experimental work, have proven fundamental in gaining insight into these mechanisms resulting in the formulation of several different hypotheses, however current models of mammalian nerves still do not capture all of the mechanics when compared to experimental evidence [7]. If overcome, this has the potential to refine experimental protocols thereby reducing the number of in-vivo experiments, as well as leading to power requirement reductions in implementing the technique and empowering the neuroscience community as a whole to study the technique further.

In this project, two popular models used for the investigation of HFAC nerve block have been studied, as well as a third modified version of one these models. All were constructed and tested in the NEURON simulation environment, after which results were then compared with both computational and experimental evidence found within the literature. The aim was to attempt to gain an understanding of the biophysical mechanisms underpinning these models and to assess their performance in replicating experimental findings of nerve block.

## 1.1 Modelling of Peripheral Nerve Fibres for Conduction Block

The peripheral nervous system consists of two distinct types of nerve fibre; sensory (afferent) neurons and motor (efferent) neurons. Both include three further classifications known as group A fibres, group B fibres, and group C fibres. A-fibres are the thickest and fastest conducting due to the presence of myelination, B-fibres are medium in diameter and moderately myelinated resulting in slower conduction, whilst C-fibres are smallest in diameter and unmyelinated resulting in the slowest conduction of the three. In all cases when an action potential (AP) is generated at the soma it propagates down the fibres axon(s) to the dendrites which communicate electrically with other neurons via synapses. For nerve conduction block, this electrical transmission is usually interrupted at some point along the axon, leading to conduction failure.

The modelling of all three fibre categories for nerve block in the NEURON simulation environment typically involves constructing a multi-compartmental model of a single axon. Each compartment consists of modelled electrical circuits which represent the fibres passive properties and ion channel kinetics. In a manner that mimics *in vivo* experimental design [8], an extracellular current source delivers HFAC stimulation halfway along the axon. Afterwards an intracellular test pulse is delivered to one end of the axon and the opposite end is monitored to determine if conduction block occurs.

This method has led to a variety of models being generated, all differing in fibre type, accuracy and complexity. However, there are still several different fibre types that are yet to be modelled effectively whilst existing models still require constant improvement. In particular, a recent survey of electrostimulation methods by Reilly (2016) [9] states that there is a current need for the development of models for C-fibres among other nerve types.

## 1.2 Characteristics of HFAC nerve block

The phenomenon of true nerve conduction block can be defined as a ‘quick, reversible and complete inhibition of AP propagation through the stimulated region of tissue’ [10]. HFAC ( $>1\text{kHz}$ ) stimulation delivered to a nerve via an electrode has been shown to cause conduction block through the creation of a blocking region at which AP propagation ceases to pass through. This has been demonstrated in a variety of different species and nerve diameters including that of seas slugs [11], cats [12], frogs [13], and rats [14]. In human studies, attention has been focused primarily on the vagus nerve [15], sciatic nerve, and spinal cord [16].

Tanner (1962) [17] was the first to demonstrate that nerve fibres could be blocked selectively according to their diameter. This was shown in the sciatic nerve of frogs stimulated using a 20kHz sinusoidal waveform that was modulated by amplitude. Woo and Campbell (1964) [18] confirmed his findings in both the frog sciatic and cat tibial nerves, where they were able to show that the occurrence of block was highly dependent upon two stimulation parameters; the frequency and amplitude/intensity<sup>1</sup>. The lowest intensity of stimulation necessary at a given frequency to provide block of a target nerve has since been named the block threshold.

Several other characteristic features of HFAC nerve block have been identified, one of which is the onset response. First described by Woo and Campbell (1964) [18], the onset response is described as a brief period of repetitive asynchronous firing induced upon delivery of HFAC. The issue created by this phenomenon in terms of clinical applications is that it can lead to painful muscle contractions in some instances; acting as a “side effect” of the technique. Many studies have therefore been conducted with the aim of minimising the onset response magnitude and duration. For instance, Ackermann et al (2010) [19] found that varying electrode contact spacing between the

---

<sup>1</sup> In this study, the terms amplitude and intensity are used interchangeably in the context of conduction block.

nerve (inter-electrode distance: IED) had some effect in minimising the amplitude and duration of the onset response.

Another characteristic feature of HFAC nerve block is block selectivity. First demonstrated by Joseph and Butera (2009) [11], they were the first to show that nerves of different fibre types could be blocked selectively. Across two studies on the sea slug and frog sciatic nerve respectively they found that myelinated A-fibres displayed a monotonic relationship between block threshold and frequency whereas unmyelinated C-fibres displayed a non-monotonic relationship [11], [13]. Illustrated in Figure 1-1(a) [13], there are regions in which specific amplitudes and frequencies of stimulation will selectively block only one fibre type. Similar findings have been demonstrated experimentally since [20], however to date no computational models have been able to replicate the non-monotonic block threshold curve shown in C-fibres here. The idea of selective inhibition of activity in specific fibre types is very desirable in neural stimulation therapies because this allows for more specificity and precision in the targeting of stimulation, reducing the likelihood of side effects and unwanted physiological changes as a result.

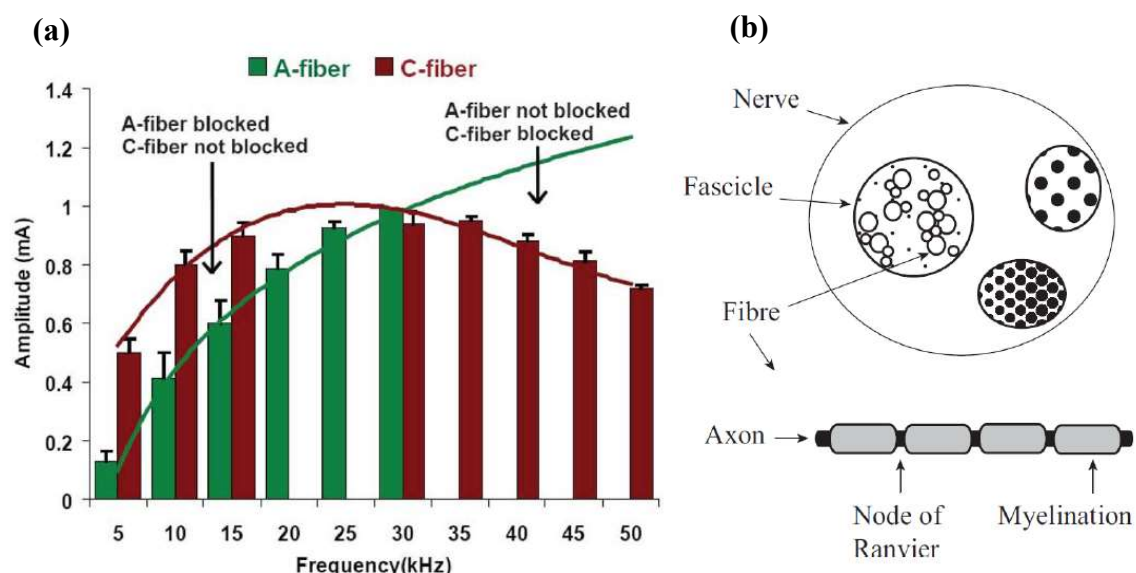


Figure 1-1: (a) Taken from Joseph and Butera (2011). Clustered column plot comparing the average block threshold for A-fibre and C-fibre components of a compound action potential produced by stimulation of the frog sciatic nerve. Noted are two regions in which different frequency-amplitude combinations allow one fibre to be selectively blocked (b) Cross section of a peripheral nerve, adapted from [7].

## 2. Methods

Three separate models were constructed; two unmyelinated fibres and one myelinated fibre. Investigations were carried out over a range of frequencies and intensities of AC stimulation, as well as three different fibre sizes and three inter-electrode distances (IEDs) for each model. This allows for a thorough examination of nerve behaviour under HFAC block across a range of variables. A summary of these primary variables for all three models as well as some further basic parameters are shown in Table 2-1. In addition, each model was subject to biphasic high-frequency stimulation with both sinusoidal and square waveforms.

Although geometrical parameters differ, the generalised setup for all simulations can be seen in Figure 2-1. The block electrode (monopolar) providing the extracellular high-frequency stimulation is situated halfway along the axons length and at an IED of either 1, 2 or 3mm. At one tenth along the axons length the test electrode is placed providing an intracellular unit pulse (pulse width: 0.12ms; intensity: 15mA) to evoke an action potential that propagates towards the site under the block electrode. The test pulse is cathodal (negative), and the HFAC current begins with the cathodal phase first.

In all three models it is assumed that the axon is in an infinite isotropic and homogenous medium (resistivity  $\rho = 300 \Omega\text{cm}$ ) [21]. Thus the small influence of the axon in the homogenous medium can be neglected, and the extracellular potential  $V_{e,n}$  at the  $n^{\text{th}}$  segment along the axon can be described by:

$$V_{e,n} = \frac{\rho_e}{4\pi} \left[ \frac{I_{block}(t)}{\sqrt{(n\Delta x - x_o)^2 + z_o^2}} \right] \quad (2.1)$$

where  $I_{block}(t)$  is the high-frequency biphasic current delivered to the block electrode at location  $x_o$ , halfway along the length of the axon, and  $z_o$ , the inter-electrode distance (1, 2 or 3mm) above the axon.

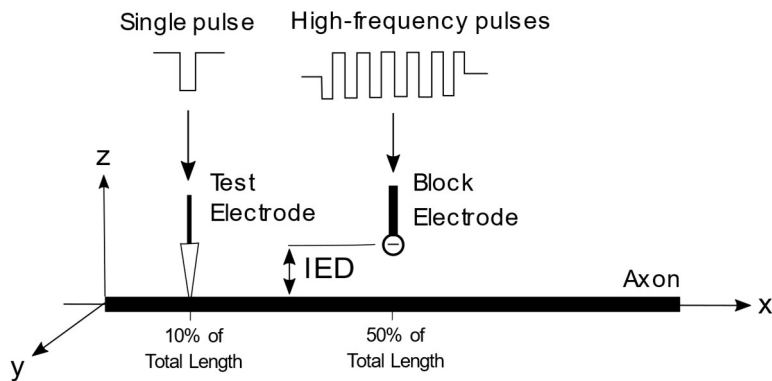


Figure 2-1: General representation of the simulation setup for all three models (adapted from [21]).

*Table 2-1: Primary variables and parameters across all three model simulations.*

Parameter/variable	Model		
	<b>H-H</b>	<b>MRG</b>	<b>C-fibre</b>
Myelination	Unmyelinated	Myelinated	Unmyelinated
Total Length (mm)	9	17.5, 26.25, 35	9
Diameters (um)	1, 2, 4	5.7, 7.3, 8.7	1, 2, 4
No. of segments	36	561	36
IED (mm)	1, 2, 3	1, 2, 3	1, 2, 3
Simulation duration (ms)	100	50	200
dt ( $\mu$ s)	1	5	1
Frequency range (kHz)	1-100kHz	1-40kHz	1-40kHz

## 2.1 H-H Unmyelinated Axon model

The first unmyelinated axon model was based on the Hodgkin-Huxley lumped circuit model [22], derived from experiments performed on the giant squid axon. This felt like a good starting point for research given the nature of its simplicity as a model, requiring less computational power, and still a popular choice for the modelling of unmyelinated fibres [21], [23], [24].

It consists of a 9mm-long single fibre axon segmented into 36 cylinders of length  $\Delta x = 0.25\text{mm}$ . Each segment is modelled by a resistance-capacitance circuit as shown in Figure 2-2(a), whereby the ionic currents passing through the membrane resistance,  $R_m$ , are described by the Hodgkin-Huxley equations (see Appendix A.1 for equations) [22].

Passive parameters include the membrane capacitance  $C_m$  which represents the separation of ions across the membrane via the lipid bilayer, and axonal resistivity  $R_a$  which represents the longitudinal flow of ions along the axon. Values used for all electrical parameters are shown in Table 2-2, taken directly from Hodgkin-Huxley (1952).

*Table 2-2: Electrical parameters for Hodgkin-Huxley model [22].*

Sodium channel max conductance ( $\bar{g}_{Na}$ )	0.12 S/cm <sup>2</sup>
Potassium channel max conductance ( $\bar{g}_K$ )	0.036 S/cm <sup>2</sup>
Leakage conductance ( $\bar{g}_l$ )	0.0003 S/cm <sup>2</sup>
Sodium reversal potential ( $E_{Na}$ )	50 mV
Potassium reversal potential ( $E_K$ )	-77 mV
Leakage reversal potential ( $E_l$ )	-54.3 mV
Membrane capacitance ( $C_m$ )	1 $\mu$ F/cm <sup>2</sup>
Axonal resistivity ( $R_a$ )	34.5 $\Omega$ cm

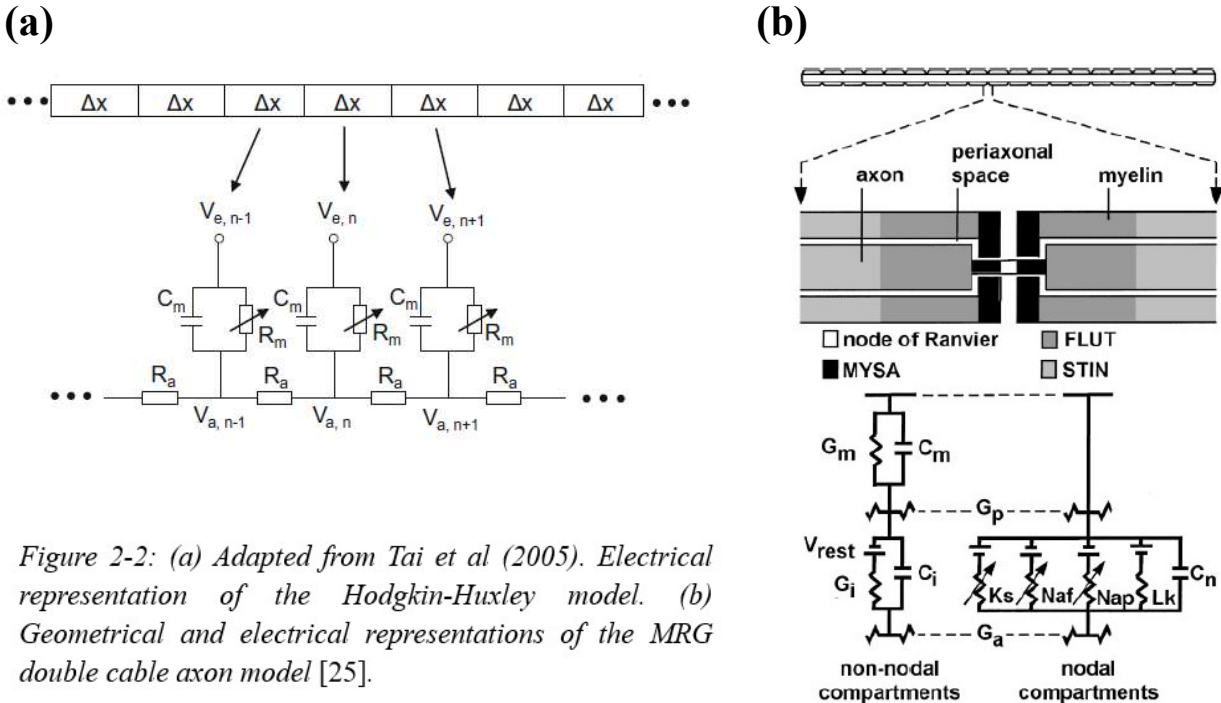


Figure 2-2: (a) Adapted from Tai et al (2005). Electrical representation of the Hodgkin-Huxley model. (b) Geometrical and electrical representations of the MRG double cable axon model [25].

## 2.2 MRG Axon Model

The second model chosen is the McIntyre-Richardson-Grill (MRG) Axon model [25], based on their study of myelinated mammalian nerve fibres. The model was able to reproduce a wide range of experimental data on the excitation properties of such nerve fibres with a particular focus on the recovery cycle, predicting depolarising (DAP) and hyperpolarising (AHP) afterpotentials that closely match experimental results [26], [15]. It is a widely used model for simulation studies on the effect of extracellular fields on myelinated mammalian axons, as well as HFAC nerve block specifically [7], [9], [27].

The MRG model (Figure 2-2(b)) is a multi-compartmental double cable model consisting here of 36 single-segment Nodes of Ranvier separated by 35 internodes. Each internode is comprised of 2 paranodal myelin attachment segments (MYSA), 2 paranodal main segments (FLUT) and 6 internodal segments (STIN), organised in the following sequence: NODE-MYSA-FLUT-STIN(x6)-FLUT-MYSA-NODE. The internodal compartments (MYSA, FLUT, STIN) are surrounded by a myelin sheath that is separated from the axon by a thin periaxonal space.

Geometrical parameters of the axon are shown in Table 2-3. As in the Hodgkin-Huxley model (henceforth: H-H model), three different fibre sizes were investigated, but in this case other geometrical parameters must be scaled to size with the fibre diameter ( $D$ ). The fibre diameter includes the thickness of the myelin sheath, which remains constant between two consecutive nodes. For further detail on the model geometry see [25]. All electrical parameters are shown in

Table 2-4. Equations for all ionic currents, as well as an overview of the membrane dynamics are shown in Appendix B.1.

*Table 2-3: Geometrical parameters for the MRG axon model [25]. All values are expressed in  $\mu\text{m}$ . MYSA, myelin attachment section of paranode; FLUT, main section of paranode; STIN, internodal section, 6 of which are in one internode.*

Parameter	Fibre size (Diameter)		
	5.7	7.3	8.7
Total fibre length ( $L$ )	17,500	35,000	40,250
Number of myelin lamella ( $nl$ )	80	100	110
Node-node distance ( $\Delta x$ )	500	750	1,000
Node length ( $L_1$ )	1	1	1
Node diameter ( $d_1$ )	1.9	2.4	2.8
MYSA length ( $L_2$ )	3	3	3
MYSA diameter ( $d_2$ )	1.9	2.4	2.8
MYSA periaxonal space width ( $p_2$ )	0.002	0.002	0.002
FLUT length ( $L_3$ )	35	38	40
FLUT diameter ( $d_3$ )	3.4	4.6	5.8
FLUT periaxonal space width ( $p_3$ )	0.004	0.004	0.004
STIN length ( $L_4$ )	70.5	111.2	152.2
STIN diameter ( $d_4$ )	3.4	4.6	5.8
STIN periaxonal space width ( $p_4$ )	0.004	0.004	0.004

*Table 2-4: Electrical parameters for MRG model [25].*

Nodal capacitance ( $C_n$ )	$2 \mu\text{F}/\text{cm}^2$
Axonal resistivity ( $R_a$ )	$70 \Omega/\text{cm}$
Fast $\text{Na}^+$ channel max conductance ( $\bar{g}_{Na_f}$ )	$3.0 \text{ S}/\text{cm}^2$
Persistent $\text{Na}^+$ channel max conductance ( $\bar{g}_{Na_p}$ )	$0.01 \text{ S}/\text{cm}^2$
Slow $\text{K}^+$ channel max conductance ( $\bar{g}_{K_s}$ )	$0.08 \text{ S}/\text{cm}^2$
Nodal leakage conductance ( $\bar{g}_l$ )	$0.007 \text{ S}/\text{cm}^2$
Sodium reversal potential ( $E_{Na}$ )	50.0 mV
Potassium reversal potential ( $E_K$ )	-90.0 mV
Leakage reversal potential ( $E_l$ )	-80.0 mV

## 2.3 C-fibre Axon Model with Ion Diffusion

As discussed in the literature review, there is a need for computational models describing electrostimulation via extracellular fields for other neuron classifications such as C-fibres. Thus for the final model an attempt was made to model the unmyelinated C-fibre based on works by Tigerholm et al (2015, 2018) [28], [29]. In these studies, focus was directed on the recovery cycle as well as the apparent activity-dependent changes in conduction velocity following a rapid train of action potentials shown experimentally in C-fibres [30], [31]. They found that their model was able to adequately reproduce the activity-dependent slowing (ADS) of axonal propagation velocity shown experimentally [28], and replicate the observed transitions in excitability from subnormal to supernormal following action potential conduction [29]. To their knowledge the model constructed for these studies was the first to address axonal propagation of action potentials in C-fibres. In this study an adapted form of the model was developed to see how it responded to extracellular HFAC stimulation. Results were then compared to that found in the literature, in particular the non-monotonic block threshold curve from Section 1.2.

Geometrically the model was set out in the same form as the H-H model, with a 9mm-long axon consisting of 36 segments. Three different fibre diameters were investigated (1,2 and 4 $\mu\text{m}$ ), with 1 $\mu\text{m}$  being the most physiologically accurate [32]. A series of Hodgkin-Huxley-type ion channels were included as well as the sodium-potassium ion pump (Na/K-ATPase), these are listed in Table 2-5 along with their respective conductances. Dynamics for the changes in sodium and potassium concentrations were also implemented, including a periaxonal space of thickness  $\theta = 29\text{nm}$ . This is illustrated in Figure 2-3. Initial ion concentrations are given in Table 2-6, as well as some further basic parameters. In addition, longitudinal diffusion of potassium and sodium was implemented in all compartments inside the axon. Equations for all ion channels and pumps, as well as those used to calculate longitudinal diffusion can be found in Appendix C.1.

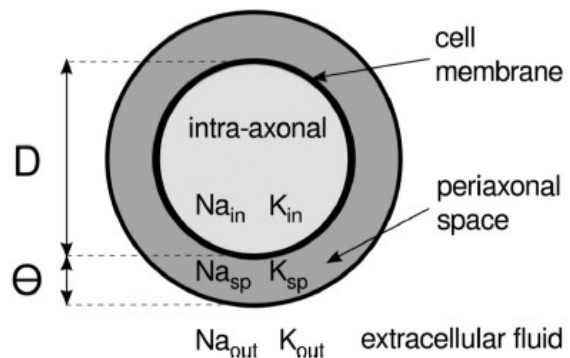


Figure 2-3: Cross-section of the axon.  $\Theta$ , width of the periaxonal space,  $D$ , diameter of the axon. Figure adapted from Tigerholm et al (2015).

Table 2-5: Channels and max conductances included in C-fibre model [28].

Channel	Max Conductance ( $\text{mS/cm}^2$ )
Sodium-potassium pump, Na/K-ATPase ( $\bar{g}_{\text{pump}}$ )	0.0048
Voltage-gated sodium channel, $\text{Na}_v1.7$ ( $\bar{g}_{\text{Na}v1.7}$ )	106.6439
Voltage-gated sodium channel, $\text{Na}_v1.8$ ( $\bar{g}_{\text{Na}v1.8}$ )	242.7124
Voltage-gated sodium channel, $\text{Na}_v1.9$ ( $\bar{g}_{\text{Na}v1.9}$ )	0.0948
Delayed-rectifier potassium channel, $\text{K}_{\text{dr}}$ ( $\bar{g}_{\text{Kdr}}$ )	18.0017
A-type potassium channel, $\text{K}_A$ ( $\bar{g}_{\text{KA}}$ )	12.7555
M-type potassium channel, $\text{K}_M$ ( $\bar{g}_{\text{KM}}$ )	6.9733
HCN channel, $h$ ( $\bar{g}_h$ )	2.5377
Sodium-activated potassium channel, $\text{K}_{\text{Na}}$ ( $\bar{g}_{\text{KNa}}$ )	0.0012

Table 2-6: Basic parameters of the C-fibre model.

Parameter	Value
Membrane capacitance ( $C_m$ )	$1 \mu\text{F}/\text{cm}^2$
Axonal resistivity ( $R_a$ )	$35.4 \Omega\text{cm}$
Sodium temperature coefficient ( $Q10_{\text{Na}}$ )	2.5
Potassium temperature coefficient ( $Q10_K$ )	3.3
Initial intracellular sodium concentration ( $\text{Na}_{in}$ )	11.4 mM
Initial periaxonal space sodium concentration ( $\text{Na}_{sp}$ )	154 mM
Extracellular sodium concentration ( $\text{Na}_{out}$ )	154 mM
Initial intracellular potassium concentration ( $\text{K}_{in}$ )	121.7 mM
Initial periaxonal space potassium concentration ( $\text{K}_{sp}$ )	5.6 mM
Extracellular potassium concentration ( $\text{K}_{out}$ )	5.6 mM

## 2.4 Simulation setup

Model equations for all three models were solved using the backward Euler method. For both unmyelinated models a fixed timestep of  $1\mu\text{s}$  was chosen, whereas for the MRG model a timestep of  $5\mu\text{s}$  was chosen as a result of the increased computational load. The H-H model had a simulation duration of 100ms, with the HFAC stimulation turned on at 5ms and the test pulse at 50ms. The MRG model simulations had a duration of 50ms with the HFAC stimulation turned on at 5ms and the test pulse at 35ms. Finally, the C-fibre model had simulation duration of 200ms, with the HFAC stimulation turned on at 5ms and the test pulse at 100ms. The reason for the difference in simulation durations is due to the decreased conduction velocity of the unmyelinated fibres, meaning it took longer for the membrane to reach steady state under the HFAC stimulation. To see an overview of all simulation parameters, revert back to Table 2-1.

### 3. Results

#### 3.1 Demonstration of block

Figure 3-1 shows the successful conduction block of the unmyelinated Hodgkin-Huxley axon model, induced by 10kHz AC stimulation. In Figure 3-1(a) the HFAC stimulation at an intensity of 88mA generates an initial AP under the block electrode, recognised as the onset response. This AP can be seen to propagate in both directions down the axon. The membrane potential under the block electrode oscillates (repetitively depolarising and hyperpolarising), with the amplitude of oscillations rapidly decreasing as we move further away from either side of the block electrode. After 10ms a single pulse is delivered from the intracellular test electrode initiating an AP that propagates down the axon towards the block electrode. This second AP fails to propagate through the site under the block electrode due to the presence of HFAC stimulation. Conversely, at a lower intensity of 87mA block is seen to fail (Figure 3-1(b)). The second AP is shown to propagate through the site under the block electrode and continue to the furthest end of the axon. Demonstrations of block in the same format as Figure 3-1 for both the MRG and C-fibre models can be found in Appendix B.2 and C.2 respectively. Furthermore, a model comparison of the H-H and C-fibre AP waveforms can be found in Appendix C.3.

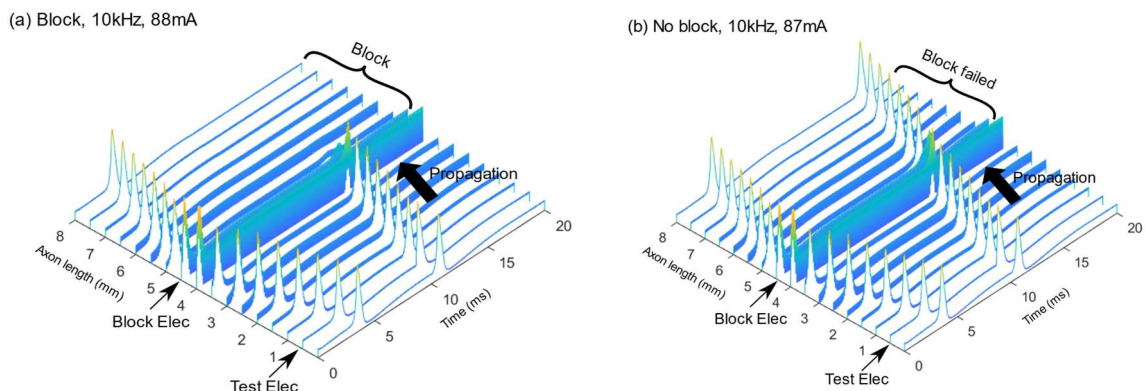


Figure 3-1: Block of action potential propagation along the unmyelinated axon by HFAC stimulation (10kHz). x-axis: Time (ms), y-axis: Distance along axons length (mm), z-axis: Membrane potential (mV). AC stimulation is delivered at the block electrode which initiates an AP (the onset response). After the response to HFAC stimulation has reached steady state (10ms) another AP is initiated at the test electrode and propagates towards the furthest end of the axon. At an intensity of 88mA the 10kHz stimulation blocks nerve conduction (a), but not at 87mA (b). Axon diameter: 2 $\mu$ m.

### 3.2 Block threshold curves

Figure 3-2 shows the block threshold over a range of frequencies (1-40kHz) of AC stimulation for a series of different simulations ran with both the H-H and C-fibre models. For all simulations a complete and reversible block was observed for all frequencies above 5kHz. Below this frequency both model axons were found to fire continuously at all amplitudes tested.

In Figure 3-2(a) the block threshold curves for both models with three different diameters are presented: 1, 2 and 4 $\mu$ m. All three simulations are conducted with an IED of 1mm. For both models at all three diameters, a linear increase in block threshold is seen with increasing frequency (starting at 6kHz); higher frequency AC stimulation is found to require a higher intensity in order to achieve conduction block. Furthermore, for the H-H model as diameter increases block thresholds decrease indicating that a larger diameter axon requires lower intensity stimulation to achieve block. The C-fibre seems to produce similar results for 2 and 4 $\mu$ m, but with a steeper gradient in block threshold in comparison to the H-H model. This increase in block threshold with fibre diameter is consistent with an increase in conduction velocity with fibre diameter, displayed in Table 3-1. Interestingly though, the 1 $\mu$ m C-fibre is shown to produce an almost identical threshold curve to the 2 $\mu$ m C-fibre, which is inconsistent with all results regarding diameter and block threshold in this study. For the MRG model, results showed the same reduction in block threshold with increasing diameter, however the intensity ranges for block across all frequencies were two orders of magnitude lower than both unmyelinated models (MRG: 0.5-3mA vs Unmyelinated: 20-450mA across all frequencies and diameters). Furthermore, a direct relationship between block effectiveness and the depolarisation level at the paranode adjacent to the Node of Ranvier under the block electrode was found in the MRG model (see Appendix B.3 for figures).

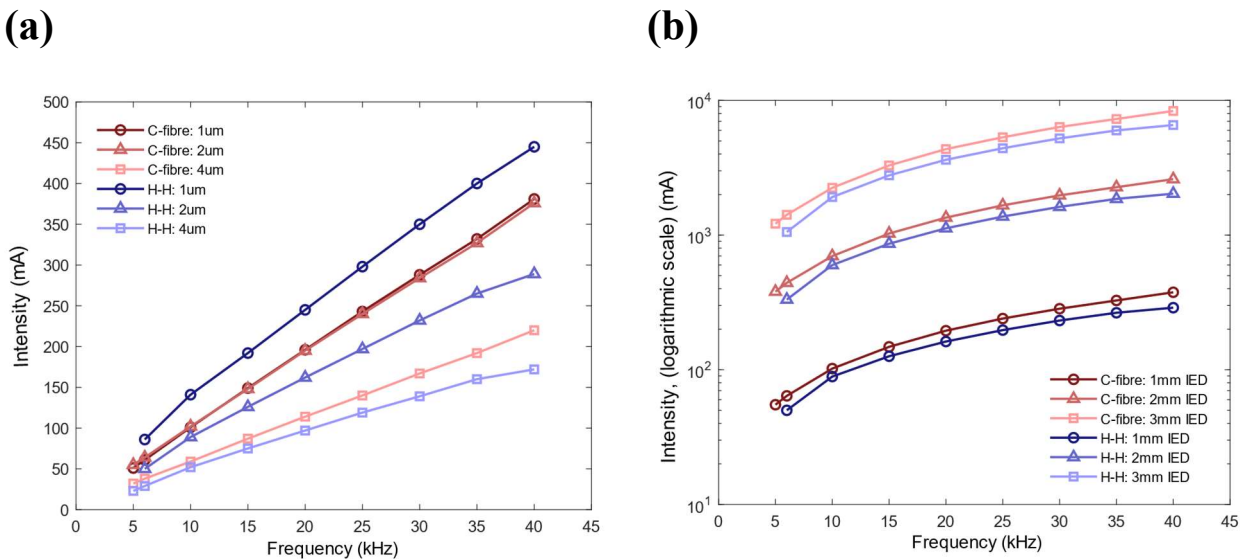


Figure 3-2: (a) Block threshold curves for C-fibre (red) and H-H (blue) models of 1, 2 and 4 $\mu$ m (b) Block threshold curves for C-fibre and H-H models under stimulation at an IED of 1, 2 and 3mm. Intensity is on a logarithmic scale. For both graphs, frequencies investigated range from 5-40kHz.

*Table 3-1: Conduction velocities for all models at each fibre diameter tested.*

Model	Conduction velocity (m/s)		
	Diam = 1µm	Diam = 2µm	Diam = 4µm
<b>H-H</b>	0.7753	1.1648	1.7204
<b>C-fibre</b>	0.1762	0.3461	0.5552
	Diam = 5.7µm	Diam = 7.3µm	Diam = 8.7µm
<b>MRG</b>	24.3056	36.4583	48.6111

Figure 3-2(b) shows the block threshold curves for simulations ran with both the H-H and C-fibre models at an IED of 1, 2 and 3mm. For all simulations the diameter of the axon is fixed at 2µm. An increase in IED is shown to produce a considerable increase in block threshold: for the H-H model, at an IED of 1mm intensity thresholds for block range from 50-161mA over the range of 6-20kHz, for an IED of 3mm block thresholds range from 1054-3623mA for the same frequency range. This increase in threshold range with increasing IED was found to display a logarithmic relationship. Viewed in this manner its shown that the threshold curves appear remarkably similar, differing only in their span across different orders of magnitude. The C-fibre model produces very similarly shaped curves at all diameters, but with a slightly raised block threshold across all frequencies for all three IEDs. For the MRG model, a similar logarithmic relationship was found, but at two orders of magnitude lower than the unmyelinated models. Unlike the unmyelinated models however, which for the same simulations produced only one distinguishable block threshold curve, the MRG axon model is shown to produce multiple regions where conduction block can be achieved when IED is increased (see Appendix B.3 for figures).

Simulations for all three models were also conducted with square waveform AC stimulation (see Appendix A.2 and B.3 for figures). This resulted in a lower block threshold curve than sinusoidal waveform stimulation, however multiple specific frequencies above 5kHz resulted in repetitive firing over a large range of intensities which was not seen with the sinusoidal waveform.

Finally, for both unmyelinated models there were two cases found in which the onset response could be suppressed. The first of these was achieved by administering anodal (positive phase first) AC stimulation rather than cathodal (see Appendix A.3 for figure). The second case was found specifically with the 1µm C-fibre model (see Appendix C.4 for figure). For both cases the onset response could be suppressed between certain intensity ranges, and as frequency increased these ranges increased in size.

### 3.3 Mechanisms for block

#### 3.3.1 Hodgkin-Huxley model

Figure 3-3 shows results from the same simulation as Figure 3-1(a) (10kHz and 88mA AC stim) but looks in detail at the variation in membrane potential, ionic currents, and ion channel gating

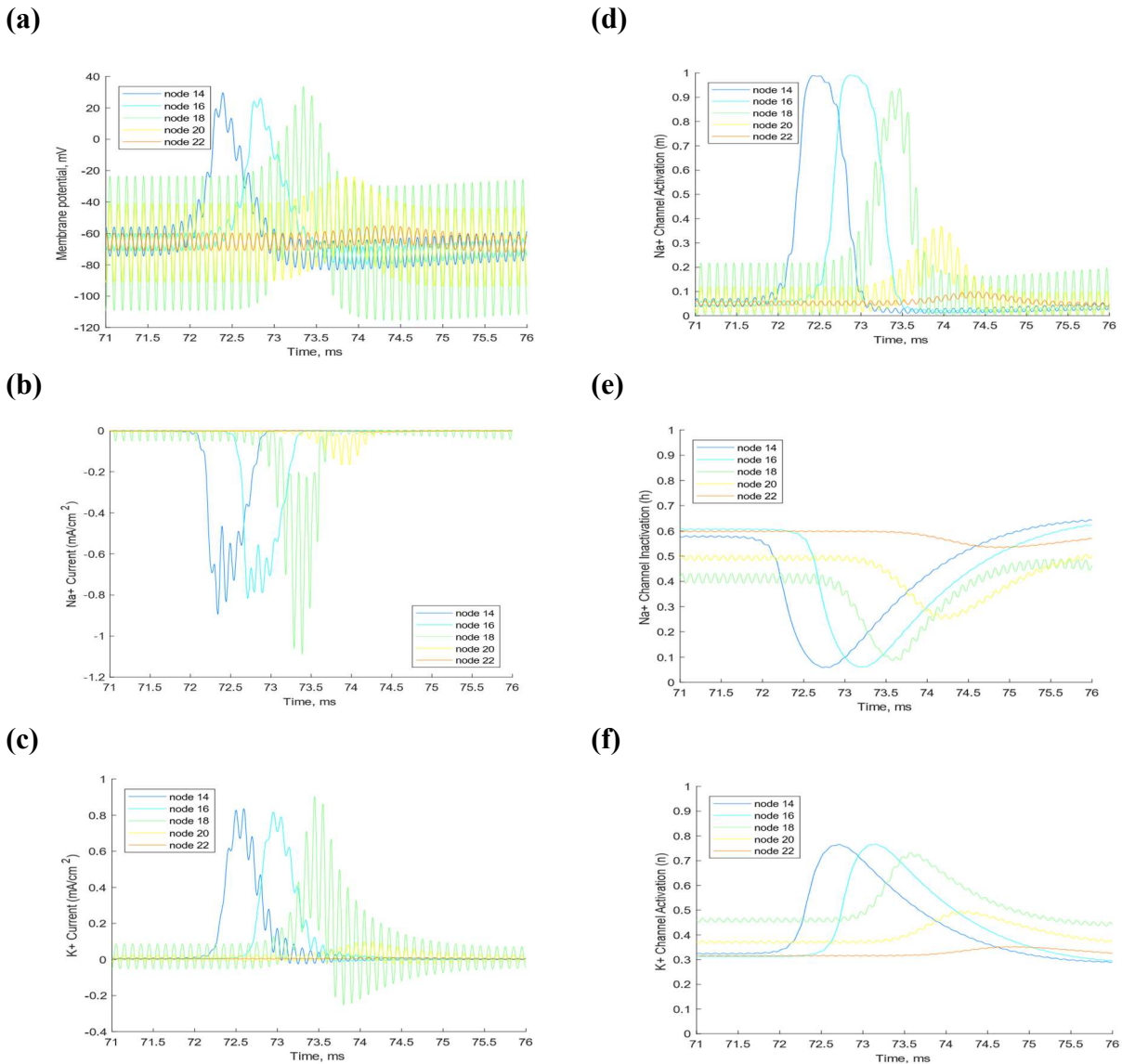


*Figure 3-3: Simulation is for 10kHz stimulation at 88mA, above block threshold (a) Membrane potential (b) Sodium current (c) Potassium current (d) Sodium activation, m (e) Sodium inactivation, h (f) Potassium activation, n. All graphs show five nodes in close proximity to the blocking electrode over the 5ms in which block occurs. Node 18 (green) is directly under the block electrode, node 14 (blue) is before and node 22 (red) is after.*

variables of five axon segments (henceforth: nodes<sup>2</sup>) in close proximity to the blocking electrode. Node 14 and 16 are situated to the left of the blocking electrode, node 18 is directly under the blocking electrode, and node 20 and 22 are situated to the right of the blocking electrode. This variation is shown over a short timescale (5ms) in which the AP generated by the test pulse is

---

<sup>2</sup> Here “Node” refers to the internal centre of each segment/compartment in the axon model, as opposed to Nodes of Ranvier referenced in the MRG Axon model.

propagating through node 14 and 16 before being blocked at node 18. In Figure 3-3(a), the AP propagation in terms of membrane potential is disrupted under the blocking electrode, where large oscillations in membrane potential can be seen as noted previously (Figure 3-1). This is consistent with large pulsed sodium and potassium currents shown in Figure 3-3(b-c).

Further explanation of the membrane potential behaviour can be derived from the gating variables of the sodium and potassium channels (Figure 3-3(d-f)). As the AP propagates towards the blocking electrode the sodium activation variable ( $m$ ) changes and becomes slightly weaker and oscillatory under the blocking electrode (Figure 3-3(d)). The sodium inactivation variable ( $h$ ) is found to increase very slightly (roughly to 0.1) under the block electrode whilst also becoming slightly oscillatory (Figure 3-3(e)). This combination of variables shows that the sodium channels are never completely closed when block occurs and leads to the pulsed inward current seen in Figure 3-3(b). As for the potassium activation variable ( $n$ ), the increase in value resulting from the AP becomes slightly smaller and oscillatory under the block electrode compared to elsewhere (Figure 3-3(f)), leading to a pulsed outwards potassium current (Figure 3-3(c)). Noticeably, despite the weakening of all three channels under the block electrode this results in increased, albeit oscillatory, sodium and potassium currents compared to elsewhere in the axon. It seems that this can be explained by the steady state achieved under HFAC stimulation: Before the AP arrives at node 18, sodium activation is at an increased level of oscillation (approximately a peak of 0.2 at node 18 compared to 0.07 at node 14), however this is offset by an increased level of sodium inactivation (approx. 0.4 at node 18 compared to 0.6 at node 14) and an increased level of potassium activation (approx. 0.47 at node 18 compared to 0.3 at node 14), resulting in a state of tonic depolarisation. When the AP arrives the longer time constants of both  $n$  and  $h$  in comparison to  $m$  must be considered. The fast increase in sodium activation is offset by the already increased steady state values of potassium activation and sodium inactivation. The combination of the sodium channel variables results in a sodium influx with a higher peak than elsewhere in the axon but with deeper oscillations due to the increased inactivation. For potassium, this leads to an increased current large enough to counteract the sodium current resulting in the block of action potential conduction.

Figure 3-4(a-c) shows how the ion channel gating variables under the block electrode change with differing frequency and a fixed intensity (100mA) at the arrival of the AP. All frequencies of stimulation except 12kHz achieved conduction block. For the sodium activation variable, a lower frequency results in an increased level of oscillation at steady state (Figure 3-4(a)). The inactivation variable maintains a decreased value (increased inactivation) with a lower frequency (Figure 3-4(b)), whilst for the potassium activation variable a lower frequency can maintain a higher activation level (Figure 3-4(c)), explaining why lower frequencies of AC stimulation have a lower blocking threshold as indicated in Figure 3-2: For the lower frequencies at which block occurs (8,9,10,11kHz), despite the increased pulsed activation of sodium the increased inactivation of sodium (reduction in  $h$ ) and high activation of potassium results in a potassium current that opposes the sodium current strongly enough to block conduction. For the higher frequency of 12kHz however, the activation of potassium and inactivation of sodium are just below threshold to effectively cancel out the inward sodium current, resulting in transmission. The threshold for potassium activation appears to be at or above roughly 0.45, whereas for sodium inactivation 0.41

or below.

Figure 3-4(d-f) shows how the ion channel gating variables under the block electrode change with differing intensities of HFAC stimulation and a fixed frequency of 10kHz at the arrival of the AP. The 10kHz stimulation blocks conduction at amplitudes of 90mA and above, which again corresponds to a potassium activation level of roughly 0.45 and sodium inactivation level of roughly 0.41. Sodium activation increases in oscillation at steady state with increasing intensity, whilst inactivation decreases in level and potassium activation increases in level. At intensities of 90mA and above, the potassium current is large enough due to the increased and decreased levels of  $n$  and  $h$  respectively to cancel out the sodium current and block conduction.

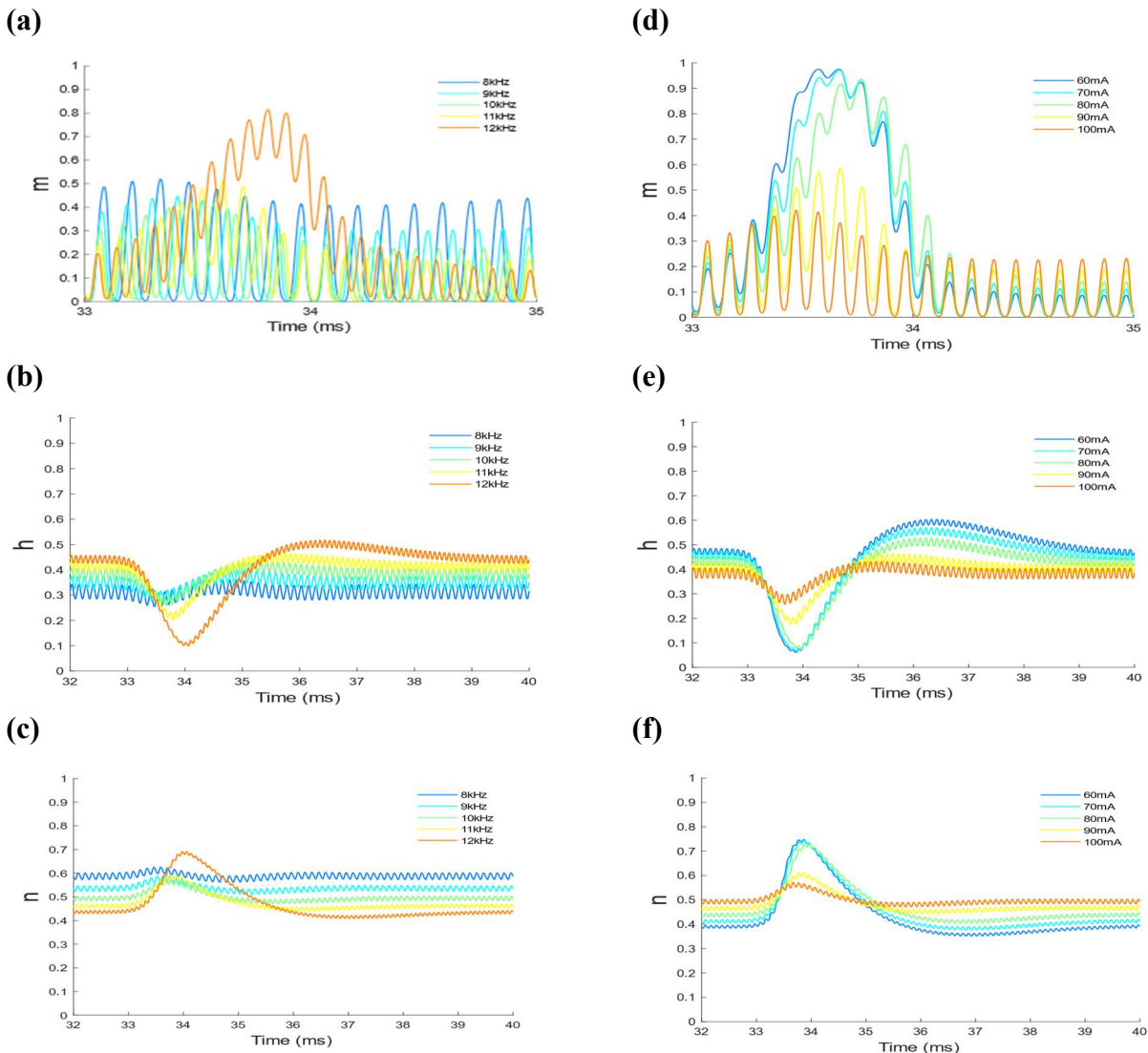
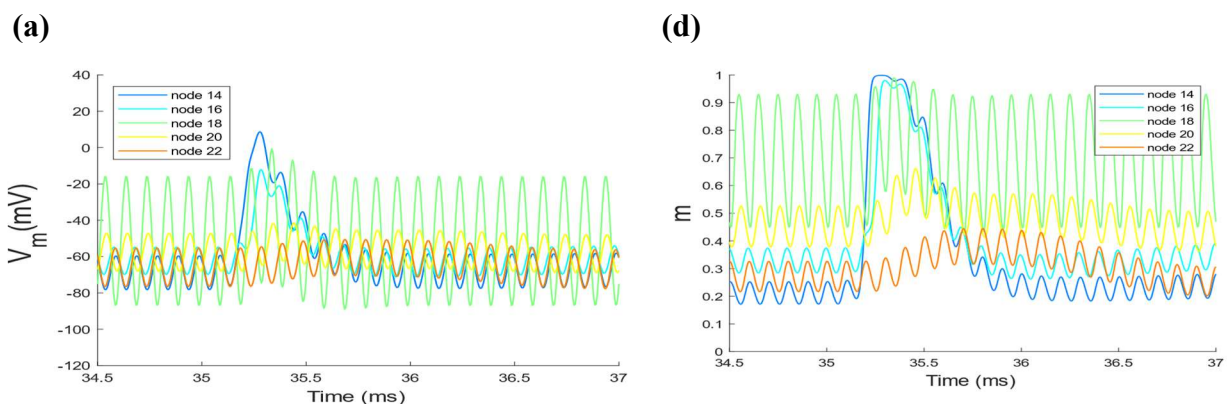


*Figure 3-4: (a-c) ion channel gating variables for the segment under the block electrode (node 18) at five frequencies of stimulation; 8, 9, 10, 11, 12kHz, and a fixed intensity; 100mA. Block at 8, 9, 10, 11kHz. No block at 12kHz. (a) sodium activation,  $m$  (b) sodium inactivation,  $h$  (c) potassium activation,  $n$  (d-f) ion channel gating variables for the segment under the block electrode (node 18) at five intensities of stimulation; 60, 70, 80, 90, 100kHz, and a fixed frequency; 10kHz. No block at 60, 70, 80mA. Block at 90, 100mA. (d) sodium activation,  $m$  (e) sodium inactivation,  $h$  (f) potassium activation,  $n$ . Time scale is during period of block.*

### 3.3.2 MRG model

The same investigation as shown in Figure 3-3 was conducted for the MRG model ( $5.7\mu\text{m}$ , 1mm IED) under conduction block at 10kHz and 1.6mA (Figure 3-5). It should be noted that here we are looking at Nodes of Ranvier, rather than internal (computational) nodes as in the two unmyelinated models. Similarly to the H-H model, under the block electrode (node 18) large oscillations in membrane potential are seen (Figure 3-5(a)), again consistent with large pulsed potassium and sodium currents (Figure 3-5(b-c)). Notice that the amplitude of the oscillating currents are considerably larger in the MRG model comparatively to the H-H model as result of the increased conductance due to myelination. Interestingly, when the AP arrives at the blocking electrode a spike in the fast sodium current is not seen under the block electrode, with sodium pulses reducing briefly in amplitude. This was not seen with the H-H model. An increase in the slow potassium current is still seen but remains strongly oscillatory.

This behaviour can be somewhat explained looking at the channel gating variables (Figure 3-5(d-f)). After the onset response has occurred the fast sodium activation ( $m$ ) reaches a steady state in which it oscillates between roughly halfway open (0.48) and fully open (0.92) (Figure 3-5(d)), whilst the inactivation variable ( $h$ ) oscillates at a low level only slightly open ( $\sim 0.04-0.05$ ) and comparatively lower than elsewhere in the axon (Figure 3-5(e)). Meanwhile the slow potassium activation ( $s$ ) reaches a steady state that is considerably higher under the block electrode than elsewhere (roughly 0.82 under the block electrode) (Figure 3-5(f)). Similarly to the H-H model, when the AP arrives at the blocking electrode it seems that the potassium activation and sodium inactivation variables are just above certain thresholds to allow for the counterbalancing of the inwards sodium current with the outwards potassium current, resulting in conduction block. Attention should also be directed to the comparatively longer time it takes for the slow potassium activation to reach steady state from the onset of HFAC stimulation (Figure 3-5(f)). This explains the onset response: when HFAC stimulation begins the sodium current is considerably higher than potassium leading to a sudden depolarisation of the membrane. Once the slow potassium activation begins to increase, the potassium current offsets the sodium current leading to a steady state of



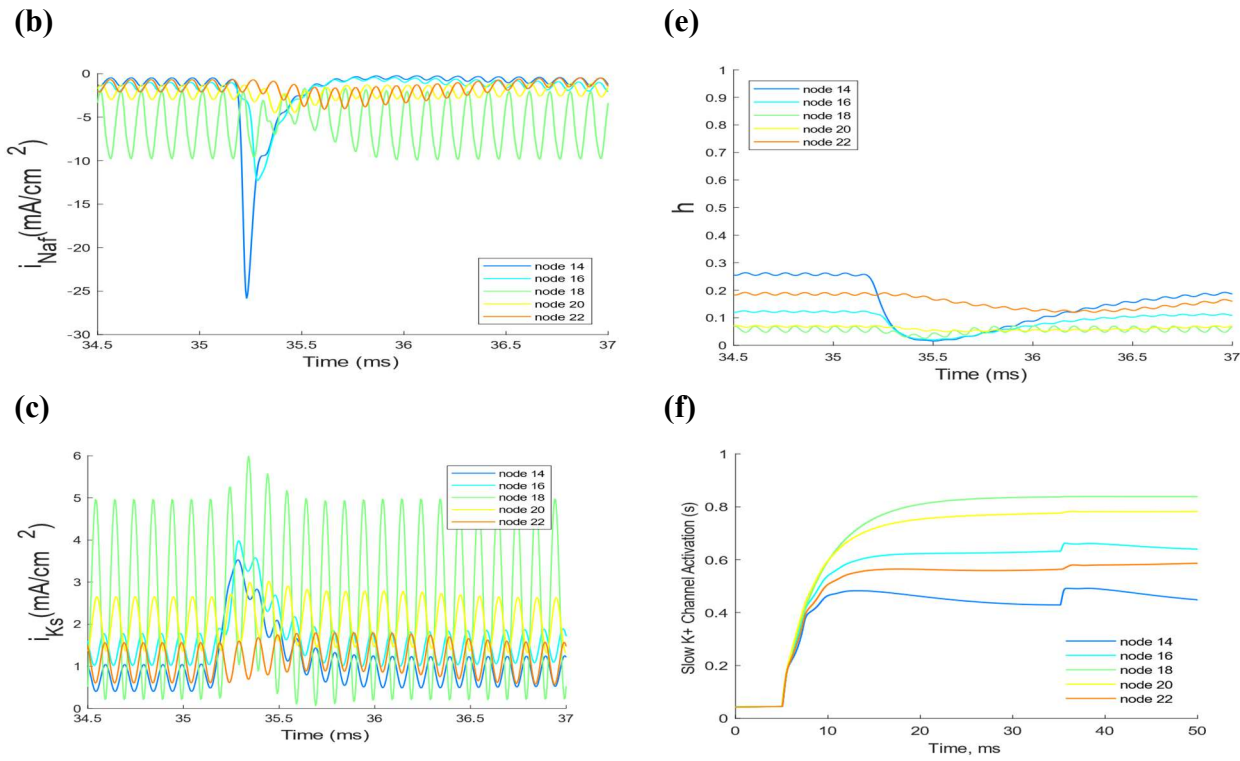


*Figure 3-5: Simulation is for 10kHz stimulation at 1.6mA, above block threshold (a) Membrane potential (b) Sodium current (c) Potassium current (d) Fast sodium activation,  $m$  (e) Sodium inactivation,  $h$  (f) Slow potassium activation,  $s$ . All graphs show five Nodes of Ranvier in close proximity to the blocking electrode over the 2.5ms in which block occurs, except for (f) which shows the change in slow potassium over the entirety of the simulation. Node 18 (green) is directly under the block electrode, node 14 (blue) is before and node 22 (red) is after.*

average depolarisation. Furthermore, it should be noted that the lack of a spike in sodium current at the onset of the AP suggests that the sodium inactivation variable plays a somewhat more significant role in generating block in comparison to the H-H model.

An investigation in the same manner shown in Figure 3-4 was conducted for the MRG model, however paranodal membrane potential adjacent to the central node was also studied. Results of this found a potassium activation threshold of approximately 0.84 and above, and a paranodal membrane voltage threshold of approximately -62mV (see Appendix B.4).

### 3.3.3 C-fibre model

The same investigation as shown in Figure 3-3 was conducted for the C-fibre model (2 $\mu\text{m}$ , 1mm IED) under conduction block at 10kHz and 102mA (Figure 3-6). In this case however, the sodium and potassium concentrations were also monitored. Like the H-H and MRG models, large oscillations in membrane potential can be seen under the block electrode (node 18), corresponding with large pulsed sodium and potassium currents (Figure 3-6(b-c)). Interestingly the oscillations in membrane potential at steady state displayed a net hyperpolarisation under the block electrode, something not seen in either of the other models (see the magnified graphic in Figure 3-6(a)).

Looking at the influence of specific ion channels it was found that the NaV1.7 and NaV1.8 voltage-gated sodium channels contributed to the vast majority of the sodium current, whilst the potassium delayed-rectifier ( $K_{dr}$ ) contributed mostly to the total potassium current with a smaller influence from the A-type potassium channels ( $K_A$ ). Given the channel conductances listed in Table 2-5, this was expected to be the case.

Further explanation of the C-fibre model behaviour during conduction block was found looking at the gating variables of these ion channels that held most influence over the ionic currents. Figure 3-6(d) shows the change in sodium activation ( $m$ ) for the NaV1.8 channel over the course of the simulation. It should be noted that the change in the NaV1.7 channel was almost identical and had less effect on the overall current, so attention is focussed on just NaV1.8 here. As highlighted by the magnified graphic, when the initiation of the HFAC stimulation occurs, the increased sodium activation (resulting in the onset response AP) is briefer and slightly weaker under the block electrode compared to elsewhere. This is also the case when looking at the closing of the inactivation variable ( $h$ ) (Figure 3-6(e)), however because of the increased time constant of the inactivation variable this results in a weaker influx of sodium under the block electrode compared to elsewhere. This is highlighted in Figure 3-6(g), which shows the changes in sodium concentration inside the axon for the same 5 segments. The same occurs with the activation variable ( $n$ ) of the potassium delayed-rectifier channel. As shown in Figure 3-6(f) the increased effects induced by the HFAC stimulation felt directly under the block electrode results in a shorter activation of the channel leading to a smaller outflux of potassium into the periaxonal space shown in Figure 3-6(h). Similarly to the H-H model, after the onset response has passed the activation of the delayed-rectifier channel reduces to an increased steady-state under the block electrode compared to elsewhere in the axon. Conversely, the sodium activation at steady state shows that sodium channels are almost closed (Figure 3-6(d)), this combination resulting in the apparent tonic hyperpolarisation of membrane potential. At 100ms the test pulse generates an AP which begins to propagate down the axon, the resulting conduction block at node 18 seems to be a combination of two different factors stemming from the tonic hyperpolarised state. Firstly looking at the NaV1.8 activation, in the same way seen during the onset response the increased presence of the HFAC stimulation under the block electrode results in a shorter and weaker increase in activation. Combined with the increased delayed-rectifier potassium channel activation this results in a cancellation of currents leading to conduction block.

An investigation in the same manner as Figure 3-4 was conducted for the C-fibre model but with the NaV1.8 sodium channel and the delayed-rectifier potassium channel (see Appendix C.5). Similarly to the H-H model conduction block occurs when the activation of potassium during steady state is just above a threshold of roughly 0.48. This compares to a threshold of 0.45 for the H-H model which may explain the slightly increased block threshold curves of the C-fibre model shown in Figure 3-2.

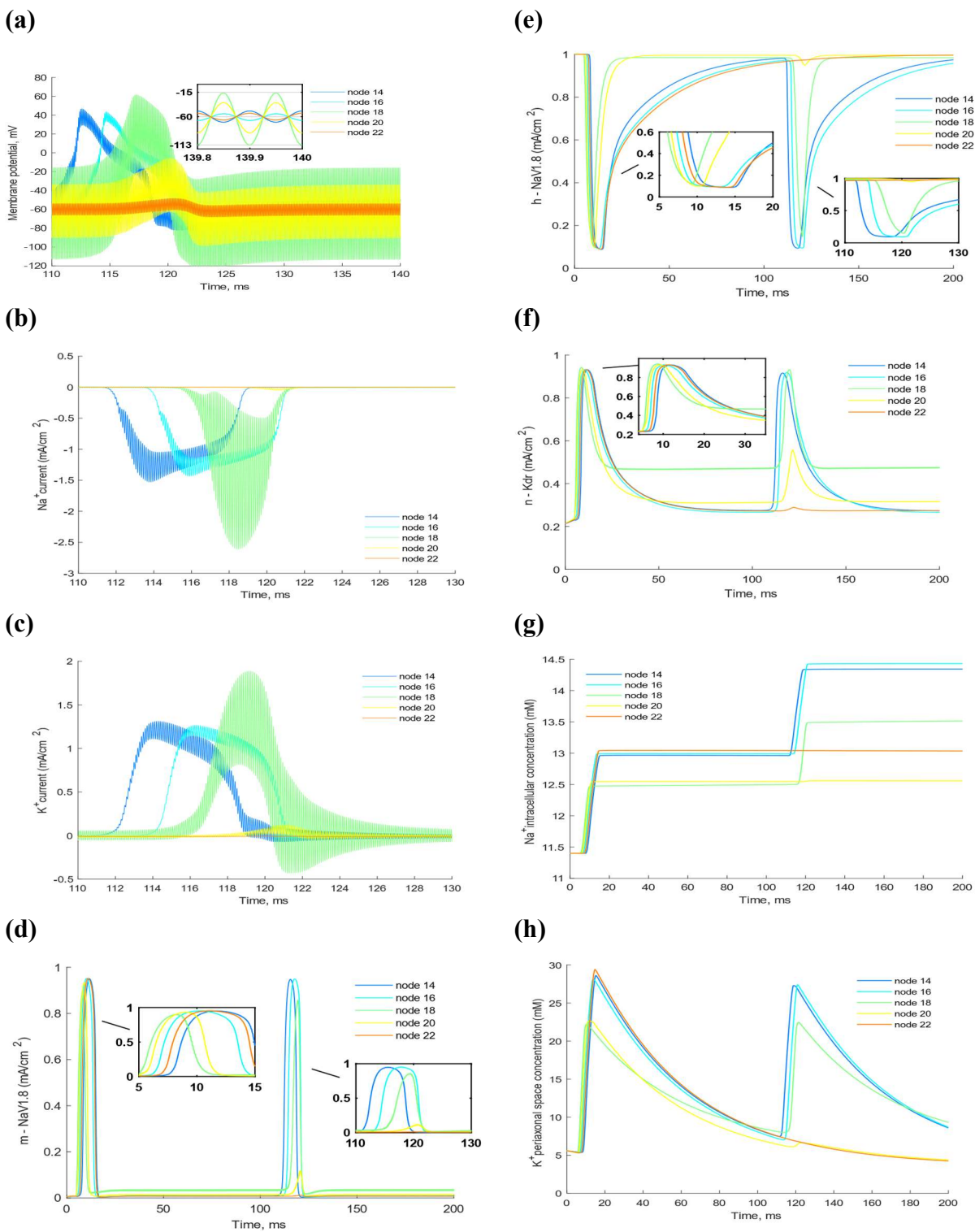


*Figure 3-6: Simulation is for 10kHertz stimulation at 102mA, above block threshold*

(a) Membrane potential  
(b) Sodium current  
(c) Potassium current  
(d)  $\text{NaV1.8}$  activation,  $m$   
(e)  $\text{NaV1.8}$  inactivation,  $h$   
(f) Potassium delayed-rectifier activation,  $n$   
(g) Intracellular sodium concentration  
(h) Periaxonal space potassium concentration. All graphs show five nodes in close proximity to the blocking electrode. Graphs (a-c) span the 20ms period in which block occurs. Graphs (d-h) span the entirety of the simulation. Node 18 (green) is directly under the block electrode, node 14 (blue) is before and node 22 (red) is after.

## 4. Discussion

### Globally investigated variables

In this study, the phenomenon of nerve conduction block induced by HFAC stimulation has been successfully simulated in three separate axon models (H-H, MRG, C-fibre). The following variables were investigated in their effects on nerve conduction block: frequency of stimulation, intensity of stimulation, fibre diameter, IED, and HFAC waveform type (sinusoidal or square). For all three models an increase in stimulation frequency required a higher intensity of stimulation to achieve block, showing a linear relationship between frequency and block threshold. This is consistent with all other computational studies of HFAC nerve block reviewed in the literature, and can be explained by the logarithmic relationship between charge per phase and HFAC frequency [10]. Interesting however, was the apparent two order of magnitude difference between intensity ranges studied of the unmyelinated models compared to the MRG model. Despite the presence of myelination and increased fibre diameter this is unlikely to explain such a difference in magnitude. Furthermore, these intensity ranges for block of the unmyelinated models are inconsistent with experimental findings [11]. This is suggestive of some form of error, however multiple studies in the literature working on similar Hodgkin-Huxley type unmyelinated models also found block was achieved over similar intensity and frequency ranges [21], [24]. Consequently the reason for such findings must be investigated further.

All three models also saw a decrease in block threshold over increasing fibre diameter, excluding the instance in which both the  $1\mu\text{m}$  and  $2\mu\text{m}$  C-fibre axon models displayed almost identical block threshold curves. Further study is required to determine why such an outcome was found. As for the remaining cases this is also consistent with results found in the literature of both computational studies [24], [12] and experimental studies on the frog sciatic nerve [17], and in cats [18]. Furthermore, it should be noted that at the lowest frequencies the block threshold was almost independent of diameter (Figure 3-2(a)), which compared well with findings that for nerve activation very long pulse widths, thus low frequencies, show minimum diameter discrimination [12], [33]. As expected the increase in diameter also saw an increase in conduction velocity across all models (Table 3-1). This is due to the increased surface area of the axonal membrane, leading to a greater number of ion channels and therefore stronger ionic currents.

For all models an increase in IED resulted in a logarithmically scaled increase in block threshold (Figure 3-2(b)). This can generally be explained by the flattening of the electric field distribution as IED increases, meaning a larger intensity is needed to achieve block. Additionally, the MRG axon model displayed multiple block threshold regions when IED was increased above  $1\text{mm}$  (Appendix B.3), something not seen among the other models. This shows that IED has a strong influence on the shape of the electric field, but also that its effects may be highly dependent on the anatomical organisation of the stimulated nerve. Research by Ackermann et al [19] and Patel et al [34] indicate that electrode configuration in general plays a crucial role in nerve conduction block. In the present study however, the modelling of the electrode/electric field and surrounding tissue were highly simplified: Only a monopolar electrode was considered, whereas bipolar or tripolar are often used experimentally, and the nerve was modelled as an isotropic material without any contact

impedance between the nerve surface and the electrode. Consequently, in future works it would be interesting to introduce a more accurate representation, for instance by modelling a bipolar (or tripolar) cuff electrode surrounding the trunk of the nerve in COMSOL Multiphysics® or SIM4LIFE, as well as including anisotropic and frequency dependent nerve properties.

Finally, all three models were subject to comparison of HFAC stimulation with sinusoidal and square waveforms (see Appendix A.2 and B.3 for figures). In all cases square wave stimulation proved to result in a lower block threshold curve, meaning square wave stimulation generally requires lower intensities to achieve conduction block. This is because if stimulated at the same intensity, square waveforms have an increased charge per phase in comparison to sinusoidal waveforms. Also found across all three models, specific frequencies of square waveform HFAC stimulation resulted in repetitive firing across broad intensity bands. The reason for this phenomenon is still unknown and no evidence of it could be found in the literature.

### **Onset response**

In some instances, a suppression of the onset response was found to be achievable (Appendix A.3 & C.4). This seems possible in the unmyelinated models because they incorporate faster acting potassium channels in comparison to the slow potassium channels implemented in the MRG model. With slow potassium channels present, the suppression of the onset response is very difficult due to the slow increase in potassium activation, allowing for large sodium influxes before steady state can be reached. In the unmyelinated models however, potassium activation upon initiation of HFAC is much quicker. For instance, in the  $1\mu\text{m}$  C-fibre model, it seems likely that the suppression of the onset response was a result of the fibres very low conduction velocity ( $0.1762\text{m/s}$ ). This meant that when HFAC was applied, despite the initial sodium influx the conduction velocity was slow enough to allow for the potassium activation to increase to a point whereby it could effectively counteract the sodium current.

### **Biophysical mechanisms**

When investigating the potential biophysical mechanisms underlying conduction block in the H-H axon model results were shown to be comparatively similar to those found in a study of the H-H model by Tai et al (2005) [24]. In this study Tai et al suggest the high activation of potassium channels maintained by HFAC as a possible mechanism for conduction block. The same conclusion was reached in this study, however here it is also believed that the increased inactivation of sodium channels should also be taken into consideration as a possible mechanism. Thus it is the combination of increased potassium activation and sodium inactivation at steady state which results in a counterbalancing of currents at the onset of the test AP, leading to block. This steady state under HFAC stimulation in which sodium channels are not completely closed leading to a pulsed inward current, but offset by an increased potassium current, seems to characterise tonic depolarisation [5].

For the MRG axon model, a similar mechanism is proposed. However as a result of the increased conduction due to myelination, ion channel gating variables behave slightly differently. Fast sodium activation oscillates at a much higher level and at larger amplitudes at steady state compared to the

H-H model, but this is offset by a comparatively increased inactivation (low  $h$ ) and increased slow potassium activation. Conclusively, the result is the same: this creates a state of tonic depolarisation whereby incoming APs are blocked by an increased sodium inactivation and potassium activation. A comparable mechanism is proposed by Bhadra and Kilgore (2004) [5].

Analysis of the C-fibre model during conduction block suggests an alternative mechanism to the two models preceding it. At steady state it appears sodium channels are almost closed under the blocking electrode, whereas delayed-rectifier potassium channels remain roughly half open at a higher level than elsewhere in the axon. This seems to result in a steady state of tonic hyperpolarisation. When an AP approaches the blocking electrode sodium influxes are slightly reduced as a result of this net hyperpolarisation, and consequently counteracted by the increased potassium current. Patel (2018) [10] mentions in his review, that himself and colleagues have conducted currently unpublished simulation studies that have found instances in which HFAC creates a region of net hyperpolarisation, but this is the only evidence of such a phenomenon that could be found in the literature.

### **Analysis of C-fibre model**

The pretext for the construction of the C-fibre model was that there is currently a lack of computational models describing extracellular electrostimulation methods for C-fibres [9]. In particular, one aspiration was to try and replicate the non-monotonic block threshold curve discovered experimentally in the findings of Joseph and Butera (2009) (Figure 1-1(a)). This was not achieved, leading to the belief that factors other than the incorporation of more biophysically accurate ion channels such as fibre geometry, extracellular media or electrode configuration may play an important role in such findings. Therefore, another ambition for further study would be to increase the complexity of the C-fibre axon model in one or more of these three avenues. Despite this, the biophysical mechanisms underlying conduction block in the C-fibre model including a steady state of tonic hyperpolarisation sets it apart from the classic H-H model, suggesting that focus on the particularity of ion channels and ion diffusion is worthwhile of study in the modelling of conduction block.

### **Improvements**

Ambitions for further works have already been mentioned, but one improvement of the present study would have been to conduct simulations with an adaptive timestep. This is because increasing frequency to high values at a fixed timestep can result in sampling errors. The result of this was that a limit had to be put on the maximum frequencies investigated in this study. For complete accuracy a variable timestep would be implemented so that the HFAC waveform consists of an equal number of samples per cycle for all frequencies.

## 5. Conclusion

In this study the following conclusions have been made:

- Block threshold has a positive linear relationship with increasing frequency. This is due to the logarithmic relationship between charge per phase and HFAC frequency and is consistent with a decrease in potassium activation with increasing frequency.
- Block threshold decreases with increasing fibre diameter.
- Block threshold increases logarithmically with increasing IED.
- Square waveform HFAC stimulation requires a lower intensity to achieve block in comparison to sinusoidal stimulation. This is due to the increased charge per phase.
- In both the H-H and MRG models, block is achieved through a steady state of tonic depolarisation in which sodium inactivation and potassium activation are increased allowing for the counterbalancing of sodium and potassium currents upon AP arrival.
- In the C-fibre model, block is achieved through a steady state of tonic hyperpolarisation in which sodium channels are almost closed and potassium activation is increased. When an AP arrives the influx of sodium is reduced and counteracted by the increased potassium current, both resulting from this hyperpolarised state.

It is difficult to ascertain whether any of the knowledge learnt here can be utilised for clinical application given that none of the models considered the complexities of fibre geometry, extracellular media, or electrode geometry and configurations, which have all been shown to affect the conditions of nerve conduction block. However, interestingly it does indicate how variations in relatively simple models can also lead to a variation in the potential mechanisms underpinning conduction block, suggesting that in a clinical setting there could also be a myriad of different biophysical mechanisms at play depending on the circumstances.

## References

- [1] C. Sköld, R. Levi, and Å. Seiger, "Spasticity after traumatic spinal cord injury: Nature, severity, and location," *Arch. Phys. Med. Rehabil.*, vol. 80, no. 12, pp. 1548–1557, 1999.
- [2] B. Amatya, F. Khan, L. La Mantia, M. Demetrios, and D. T. Wade, "Non pharmacological interventions for spasticity in multiple sclerosis," *Cochrane Database Syst. Rev.*, no. 2, pp. 2–4, 2013.
- [3] U. Buckley, R. W. Chui, P. S. Rajendran, T. Vrabec, K. Shivkumar, and J. L. Ardell, "Bioelectronic neuromodulation of the paravertebral cardiac efferent sympathetic outflow and its effect on ventricular electrical indices," *Hear. Rhythm*, vol. 14, no. 7, pp. 1063–1070, 2017.
- [4] Y. A. Patel, T. Saxena, R. V. Bellamkonda, and R. J. Butera, "Kilohertz frequency nerve block enhances anti-inflammatory effects of vagus nerve stimulation," *Sci. Rep.*, vol. 7, no. August 2016, pp. 1–11, 2017.
- [5] K. L. Kilgore and N. Bhadra, "Nerve conduction block utilising high-frequency alternating current," *Med. Biol. Eng. Comput.*, vol. 42, no. 3, pp. 394–406, 2004.
- [6] N. Bhadra and K. L. Kilgore, "High-frequency electrical conduction block of mammalian peripheral motor nerve," *Muscle and Nerve*, vol. 32, no. 6, pp. 782–790, 2005.
- [7] E. Perra, A. Rapeaux, K. Nikolic, and B. Engineering, "The Crucial Role of Nerve Depolarisation in High Frequency Conduction Block in Mammalian Nerves : Simulation Study."
- [8] A. L. Jensen and D. M. Durand, "High frequency stimulation can block axonal conduction," *Exp. Neurol.*, vol. 220, no. 1, pp. 57–70, 2009.
- [9] J. P. Reilly, "Survey of numerical electrostimulation models," 2016.
- [10] J. B. A. Patel, "Challenges associated with nerve conduction block using Kilohertz electrical stimulation To," *Biochem. J.*, vol. 1, no. May, pp. 493–505, 2018.
- [11] L. Joseph and R. J. Butera, "Unmyelinated aplysia nerves exhibit a nonmonotonic blocking response to high-frequency stimulation," *IEEE Trans. Neural Syst. Rehabil. Eng.*, vol. 17, no. 6, pp. 537–544, 2009.
- [12] N. Bhadra, E. A. Lahowetz, S. T. Foldes, and K. L. Kilgore, "Simulation of high-frequency sinusoidal electrical block of mammalian myelinated axons," *J. Comput. Neurosci.*, vol. 22, no. 3, pp. 313–326, 2007.
- [13] L. Joseph and R. J. Butera, "High-frequency stimulation selectively blocks different types of fibers in frog sciatic nerve," *IEEE Trans. Neural Syst. Rehabil. Eng.*, vol. 19, no. 5, pp. 550–557, 2011.
- [14] N. Bhadra, E. Foldes, T. Vrabec, K. L. Kilgore, and N. Bhadra, "Temporary persistence of conduction block after prolonged Kilohertz Frequency Alternating Current (KHFAC) on rat sciatic nerve.," *J. Neural Eng.*, pp. 0–15, 2017.
- [15] H. Johannessen *et al.*, "Erratum to: Vagal Blocking for Obesity Control: a Possible Mechanism-Of-Action (OBES SURG, 10.1007/s11695-016-2278-x)," *Obes. Surg.*, vol. 27, no. 1, p. 186, 2017.
- [16] C. Perruchoud *et al.*, "Analgesic Efficacy of High-Frequency Spinal Cord Stimulation : A Randomized Double-Blind Placebo-Controlled Study," vol. 2012, pp. 363–369, 2013.
- [17] J. A. Tanner, "Reversible blocking of nerve conduction by alternating-current excitation," *Nature*, vol. 195, no. 4842, pp. 712–713, 1962.
- [18] M. Woo and B. Campbell, "Asynchronous Firing and Block Peripheral Nerve Conduction by 20 Kc Alternating Current," *Bull. Los Angel. Neuro. Soc.*, vol. 29, no. 87, 1964.
- [19] D. M. Ackermann, N. Bhadra, E. L. Foldes, X. F. Wang, and K. L. Kilgore, "Effect of nerve cuff electrode geometry on onset response firing in high-frequency nerve conduction block," *IEEE Trans. Neural Syst. Rehabil. Eng.*, vol. 18, no. 6, pp. 658–665, 2010.
- [20] Y. A. Patel and R. J. Butera, "Differential fiber-specific block of nerve conduction in mammalian peripheral nerves using kilohertz electrical stimulation," *J. Neurophysiol.*, vol. 113, no. 10, pp. 3923–3929, 2015.
- [21] S. Zhao, G. Yang, J. Wang, J. R. Roppolo, W. C. De Groat, and C. Tai, "Effect of non-symmetric waveform on conduction block induced by high-frequency ( kHz ) biphasic stimulation in unmyelinated axon," pp. 377–386, 2014.
- [22] A. Huxley and A. Hodgkin, "A quantitative description of membrane current and its application to conduction

- and excitation in nerve,” *J. Physiol.*, no. 117, pp. 500–544, 1952.
- [23] C. H. Lubba *et al.*, “PyPNS : Multiscale Simulation of a Peripheral Nerve in Python,” 2018.
- [24] C. Tai, J. R. Roppolo, and W. C. De Groat, “Simulation Analysis of Conduction Block in Unmyelinated Axons Induced by High-Frequency Biphasic Electrical Currents,” *IEEE Trans. Biomed. Eng.*, vol. 52, no. 7, pp. 1323–1332, 2005.
- [25] C. C. McIntyre, A. G. Richardson, and W. M. Grill, “Modeling the Excitability of Mammalian Nerve Fibers: Influence of Afterpotentials on the Recovery Cycle,” *J. Neurophysiol.*, vol. 87, no. 2, pp. 995–1006, 2002.
- [26] B. Y. E. F. Barrett and J. N. Barrett, “Intracellular recording from vertebrate myelinated axons: mechanism of the depolarizing afterpotential,” pp. 117–144, 1982.
- [27] D. M. Ackermann, N. Bhadra, M. Gerges, and P. J. Thomas, “Dynamics and sensitivity analysis of high-frequency conduction block,” *J. Neural Eng.*, vol. 8, no. 6, 2011.
- [28] J. Tigerholm *et al.*, “Modeling activity-dependent changes of axonal spike conduction in primary afferent C-nociceptors,” pp. 1721–1735, 2013.
- [29] J. Tigerholm *et al.*, “C-Fiber Recovery Cycle Supernormality Depends on Ion Concentration and Ion Channel Permeability,” vol. 108, no. March, pp. 1057–1071, 2015.
- [30] J. . Thalhammer, S. . Raymond, F. . Popitz-bergez, and G. . Strichartz, “Modality-dependent modulation of conduction by impulse activity in functionally characterized single cutaneous afferents in the rat.,” *Somatosens. Mot. Res.*, vol. 11, pp. 243–257, 1994.
- [31] C. Weidner, R. Schmidt, M. Schmelz, M. Hilliges, H. O. Handwerker, and H. E. Torebj, “Time course of post-excitatory effects separates afferent human C fibre classes,” pp. 185–191, 2000.
- [32] D. et al Purves, *Neuroscience*. Massachusetts: Sinauer Associates, Inc., 2004.
- [33] T. J. Mortimer, “Motor Prostheses,” *Am. Physiol. Soc.*, 1981.
- [34] Y. A. Patel, S. Member, B. S. Kim, W. S. Rountree, R. J. Butera, and S. Member, “Conduction Block : Effects of Electrode Surface Area,” *IEEE Trans. Neural Syst. Rehabil. Eng.*, vol. 25, no. 10, pp. 1906–1916, 2017.
- [35] O. Obreja *et al.*, “Patterns of activity-dependent conduction velocity changes differentiate classes of unmyelinated mechano-insensitive afferents including cold nociceptors , in pig and in human,” *Pain*, vol. 148, no. 1, pp. 59–69, 2010.

# Appendices

## Appendix A – H-H axon model

### A.1 Hodgkin-huxley equations

$$I_m = C_m \frac{dV_m}{dt} + \bar{g}_{Na} m^3 h (V_m - E_{Na}) + \bar{g}_K n^4 (V_m - E_K) + \bar{g}_l (V_m - E_l) \quad (\text{A.1})$$

$$\frac{dn}{dt} = \alpha_n(V_m)(1-n) - \beta_n(V_m)n \quad (\text{A.2})$$

$$\frac{dm}{dt} = \alpha_m(V_m)(1-m) - \beta_m(V_m)m \quad (\text{A.3})$$

$$\frac{dh}{dt} = \alpha_h(V_m)(1-h) - \beta_h(V_m)h \quad (\text{A.4})$$

where  $m$  and  $h$  are the respective activation and inactivation gating variables for sodium channels,  $n$  is the activation gating variable for potassium channels,  $\bar{g}$  are the maximum conductances,  $E$  are the reversal potentials, and  $\alpha$  and  $\beta$  are the voltage-dependent rate constants.

### A.2 Sinusoidal vs Square

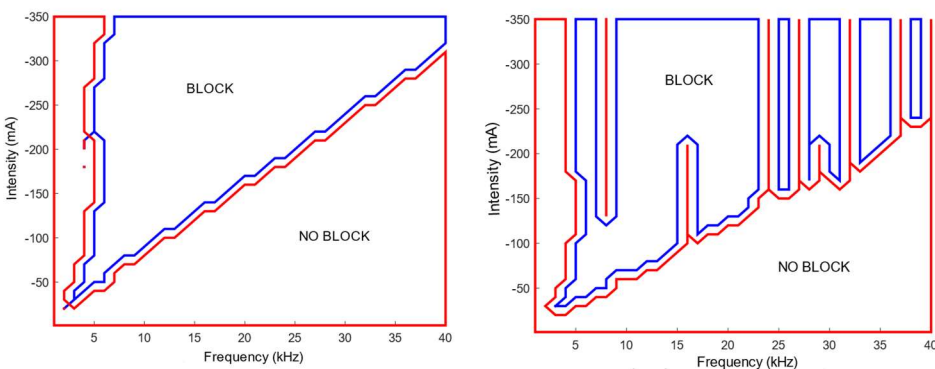


Figure A-1: Comparison between sinusoidal (left) and square (right) waveform HFAC stimulation for the H-H model. Diameter: 2 μm. IED: 1 mm. Square wave stimulation produces a lower block threshold over the range of frequencies from 4-40 kHz in comparison to sinusoidal stimulation. However, at certain specific frequencies, square wave stimulation produces repetitive firing over large ranges of intensities.

### A.3 Suppression of onset response

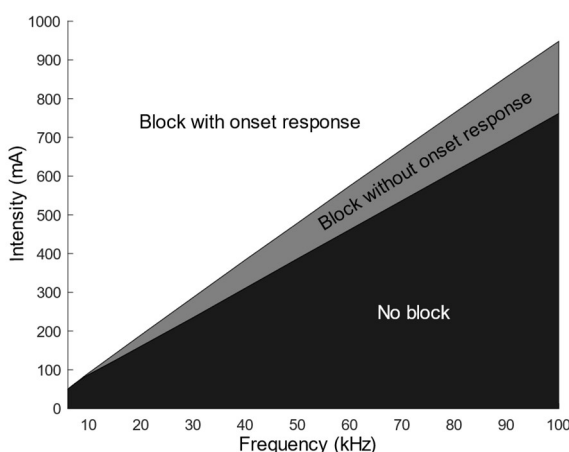


Figure A-2: Suppression of onset response via anodal HFAC stimulation. 2 μm H-H axon, 1 mm IED. Black – No block, Grey – Block without onset response, White – Block with onset response. As frequency increases the range of intensities in which block can be achieved without onset response increases.

## Appendix B – MRG axon model

### B.1 MRG membrane dynamics

As depicted in the electrical representation from Figure 2-2(b), the nodal segments are composed of both linear and non-linear circuit elements, with the non-linear elements depicting the different ion channels present. Conversely the double-layered non-nodal segments (MYSA, FLUT, STIN) only incorporate linear dynamics. The bottom layer of the circuit represents the resistive features inside the axon and the top layer represents that of the myelin sheath.

$G_a$  is the longitudinal conductivity between segments and depends on both the diameter of the segment and the axonal resistivity ( $R_a$ ):

$$G_a = \frac{R_a}{\left(\frac{d_i}{D}\right)^2} \quad (\text{A.5})$$

where  $d_i$  is the segment diameter and  $D$  is the fibre diameter. Similarly,  $G_p$  is the longitudinal conductivity in the periaxonal space, calculated by:

$$G_p = \frac{R_a}{\pi \left( \left( \frac{d_i}{2} + p_i \right)^2 - \left( \frac{d_i}{2} \right)^2 \right)} \quad (\text{A.6})$$

where  $p_i$  is the thickness of the periaxonal space associated with the segment of diameter  $d_i$ .

$G_i$  and  $C_i$  describe the passive linear dynamics of the membrane for each non-nodal segment. As in the Hodgkin-Huxley model the capacitance  $C_i$  represents the separation of ions across the membrane, and here the conductance  $G_i$  in parallel represents the small passive flow of ions across the membrane.

$$G_i = \frac{0.001}{\left(\frac{d_i}{D}\right)^2} \quad (\text{A.7})$$

$$C_i = \frac{C_n}{\left(\frac{d_i}{D}\right)^2} \quad (\text{A.8})$$

Here  $C_n$  refers to the nodal capacitance. In the same manner  $G_m$  and  $C_m$  describe the linear dynamics of the myelin sheath. Both are dependent on the number of myelin lamella (wraps) which increase with fibre diameter as shown in Table 2-3.

$$G_m = \frac{mygm}{nl \cdot 2} \quad (\text{A.9})$$

$$C_m = \frac{mycm}{nl \cdot 2} \quad (\text{A.10})$$

where  $mygm$  and  $mycm$  are the conductance and capacitance per lamella respectively, and  $nl$  is the number of myelin lamella.

At the nodal segments, slow potassium, fast sodium and persistent sodium ion channels are modelled by three different non-linear conductances;  $g_{Ks}$ ,  $g_{Naf}$ , and  $g_{Nap}$  respectively. As in the H-H model, these conductances vary depending on one or more voltage-dependent gating variables. A linear leakage conductance,  $g_L$ , is also implemented at the node. The ionic current passing through the nodal membrane can then be described by the following differential equations [25]:

$$I_m = C_m \frac{dV_m}{dt} + \bar{g}_{Naf} m^3 h (V_m - E_{Naf}) + \bar{g}_{Ks} s (V_m - E_{Ks}) + \bar{g}_{Nap} m_p^3 (V_m - E_{Nap}) + \bar{g}_l (V_m - E_l) \quad (\text{A.11})$$

$$\frac{dm}{dt} = \alpha_m(V_m)(1 - m) - \beta_m(V_m)m \quad (\text{A.12})$$

$$\frac{dm_p}{dt} = \alpha_{m_p}(V_m)(1 - m_p) - \beta_{m_p}(V_m)m_p \quad (\text{A.13})$$

$$\frac{dh}{dt} = \alpha_h(V_m)(1 - h) - \beta_h(V_m)h \quad (\text{A.14})$$

$$\frac{ds}{dt} = \alpha_s(V_m)(1 - s) - \beta_s(V_m)s \quad (\text{A.15})$$

where  $m$  and  $h$  are the respective activation and inactivation gating variables for the fast sodium channels,  $m_p$  is the activation gating variable for persistent sodium channels, and  $s$  is the activation gating variable for slow potassium channels.  $\bar{g}$  are the maximum conductances,  $E$  are the reversal potentials, and  $\alpha$  and  $\beta$  are the voltage-dependent rate constants.

### B.2 Demonstration of block - MRG

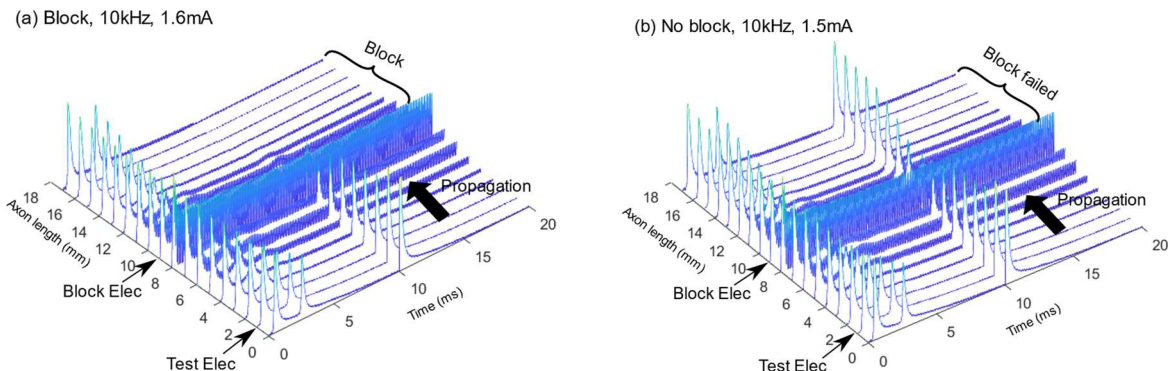


*Figure A-3: (a) The successful conduction block of the MRG axon model, induced by 10kHz stimulation. In the same manner as the H-H model an initial AP is generated through onset of HFAC stimulation, propagating down either side of the axon. The AP induced by the test electrode after 10ms is then blocked at the site of the blocking electrode. (b) Block failure. One noticeable difference between the two models is the significant reduction in intensity required to achieve block at the same frequency: 88mA for the H-H model versus 1.6mA for the MRG model. This can partly be attributed to the increased conduction of the MRG model as a result of myelination as well as the increased fibre diameter. On the other hand, this cannot be the sole reason given that the difference is so large; there must be some other factor that hasn't been taken into consideration.*

### B.3 Block threshold and paranodal average depolarisation – MRG

Much of the study of the MRG axon model was based off of works by Perra (2017) [7]. In his study a particular focus was put on the average depolarisation level under the block electrode caused by HFAC stimulation. Specifically, a direct relationship between block effectiveness and average depolarisation level (membrane potential) at the paranode adjacent to the Node of Ranvier under the block electrode was found. Figure A-4 shows the attempted replication of his findings which proved to be mostly successful:

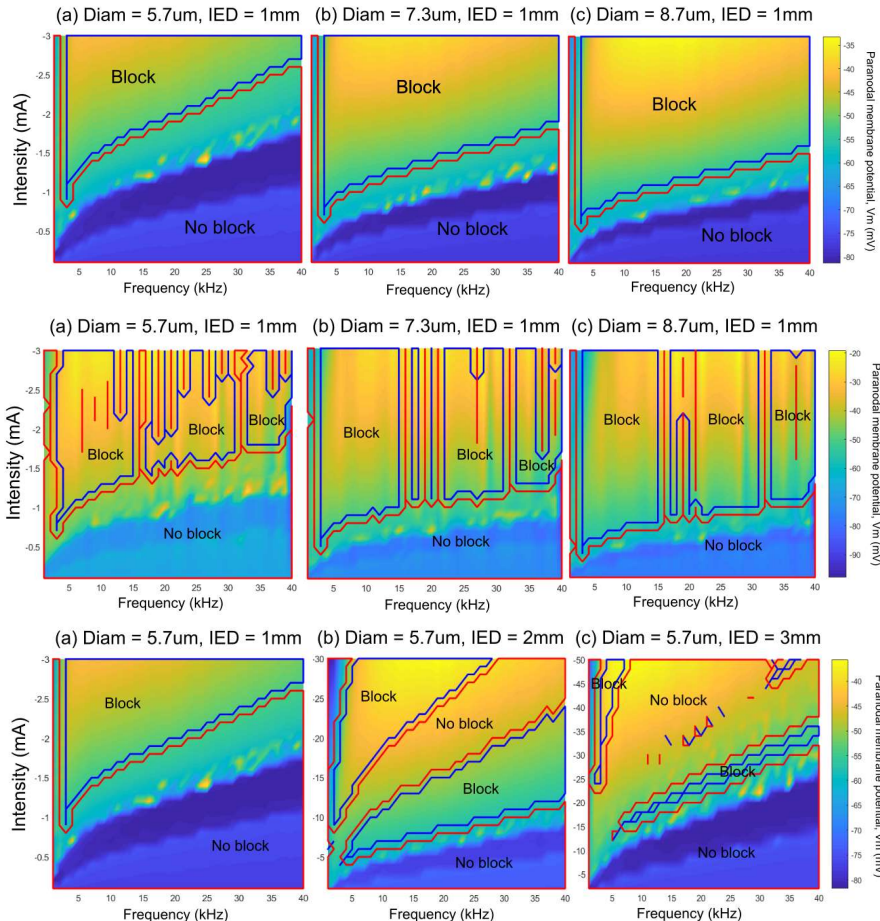


**Figure A-4:** Simulations were run over a range of frequencies (1-40kHz in steps of 1kHz) and intensities for all three fibre sizes and IEDs. A map of the average membrane potential at the paranode adjacent to the node under the block electrode (node 18) was created across all mentioned variables and superimposed with the respective block threshold curves. In terms of the paranodal membrane potential three different bands can be observed: blue and turquoise corresponding to transmission of the test AP and green and yellow corresponding to block. In the cases where block fails the paranodal membrane potential remains closer to resting potential when the intensity is particularly low,

seen as the blue band. As intensity increases there is a sharp transition into the turquoise band which corresponds to approximately a 25mV rise in paranodal membrane voltage per 0.5mA, then continuing gradually into the green band just above block threshold (~ -55 to -50mV membrane potential), and finally to the yellow band where block is firmly consolidated (~ -40 to -35mV membrane potential). In all cases the block threshold curve seems to correspond with a paranodal membrane depolarisation of approximately -60 to -55mV.

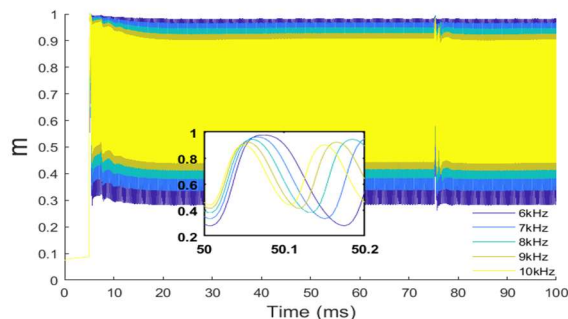
**(Top)** Looking at the change in block threshold with diameter the same trend as the H-H model is found. In all cases block threshold increases almost linearly with intensity but for larger diameter fibres the threshold curves are shifted downwards. The paranodal membrane voltage is shown to decrease consistently with this change also. Thus larger diameter fibres are easier to depolarise meaning conduction block can be achieved at lower intensities.

**(Middle)** Simulations were repeated with square waveform HFAC stimulation, resulting in a similar outcome to the H-H model whereby block threshold curves were lowered meaning a lower intensity is required to achieve block with square waveform stimulation. Multiple specific frequencies above 5kHz resulted in repetitive firing over a large range of intensities which was not seen with the sinusoidal waveform.

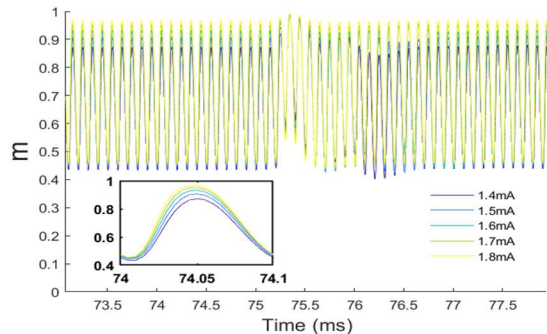
**(Bottom)** shows the same study across all three IEDs and a fixed diameter of  $5.7\mu\text{m}$ . Increasing IED generally resulted in a much higher threshold, as found with the H-H model. At 10kHz stimulation the threshold for 1mm IED is approximately 1.6mA (**left**), whilst at 2mm IED it increases to 7mA (**middle**), and 17mA for 3mm IED (**right**). Upon further investigation this proved to be a logarithmic relationship akin to the H-H model. Unlike the H-H model however, which for the same simulations produced only one distinguishable block threshold curve, the MRG axon model is shown to produce multiple regions where conduction block can be achieved when IED is increased. For instance at an IED of 2mm, two separate block regions can be distinguished (**middle**). An IED of 3mm led to two much smaller blocking regions, in contrast to Perra (2017) whose model produced an expansion of these regions.

*B.4 MRG gating variables of the central node and membrane potential of paranode adjacent to the central node for experiments with fixed frequency and fixed intensity.*

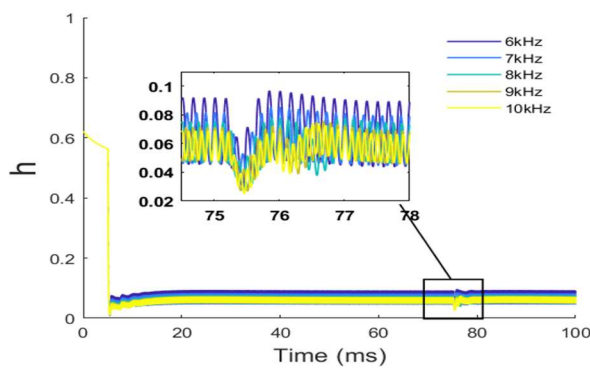
(a)



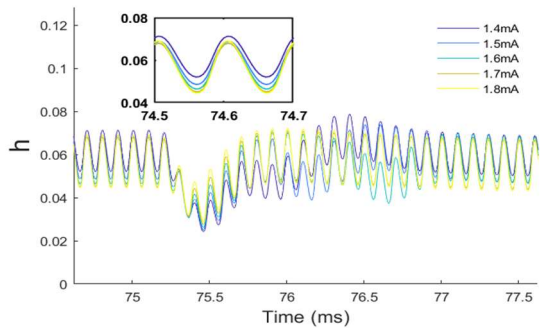
(e)



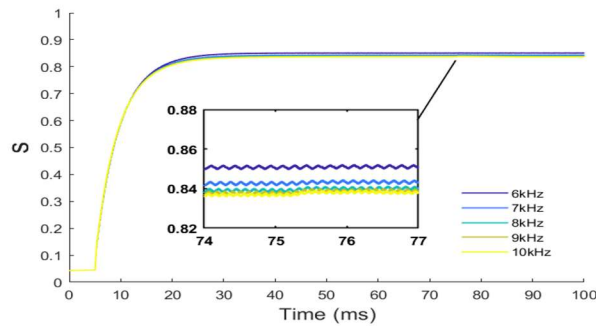
(b)



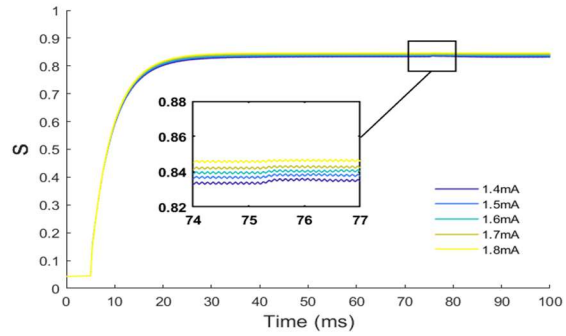
(f)



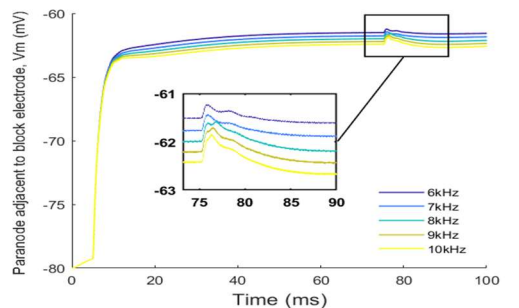
(c)



(g)



(d)



(h)

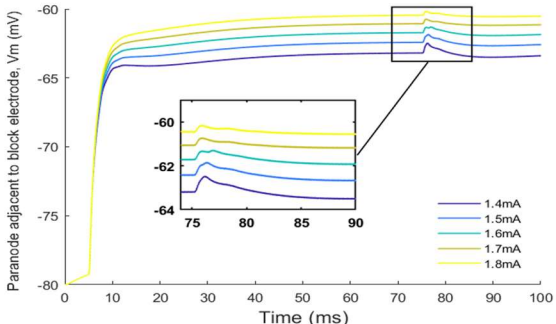


Figure A-5: (a-c) ion channel gating variables for the Node of Ranvier under the block electrode (node 18), (d) membrane voltage at the paranode adjacent to node 18. These variables are shown over the time course of the whole simulation for five different frequencies of stimulation; 6,7,8,9,10kHz, and a fixed intensity; 1.5mA. Block only at 6 and 7kHz. At steady state, sodium activation is shown to increase in amplitude of oscillations with decreasing frequency. This increase in oscillation amplitude is seen somewhat in the direction of channel opening (1) but more so towards the closing of the channel (0). For instance, comparing 6kHz and 10kHz the oscillation trough-peak are approximately 0.3-1 and 0.45-0.91 respectively. For sodium inactivation, oscillations at steady state are increased slightly towards channel opening with decreasing frequency (trough-peak: 0.42-0.64 for 10kHz and 0.42-0.85 for 6kHz). For potassium activation, decrease in frequency results in an increase in activation (from 0.84 for 10kHz to 0.85 for 6kHz), and the same is seen with paranodal membrane potential with an increase of approximately 1mV from 10kHz to 6kHz.

(e-g) the same variables are shown over the time course of the whole simulation for five different intensities of stimulation; 1.4, 1.5, 1.6, 1.7, 1.8mA, and a fixed frequency; 10kHz. Block only at intensities of 1.7mA and above. Here the relationship between each variable and changing amplitude is inverse to that of frequency. In both cases however, the threshold for block in terms of potassium activation is approximately 0.84 and above. For paranodal membrane potential, block is achieved when above approximately -62mV, which is consistent with the estimation made from Figure A-4 that suggested block was achieved at a paranodal membrane potential at or above -60mA.

## Appendix C – C-fibre axon model

### C.1 Implementation of Longitudinal diffusion

Longitudinal diffusion is dependent on the concentration gradient and governed by the first order Fick's law:

$$J = -D \frac{d\phi}{dx} \quad (\text{A.16})$$

where  $J$  is the molar flux ( $\text{mol m}^{-2}\text{s}^{-1}$ ),  $D$  is the diffusion coefficient ( $\text{m}^2\text{s}^{-1}$ ) and  $\frac{d\phi}{dx}$  is the concentration gradient along the length of the axon (x-axis). Steady-state diffusion is assumed (no change in the system with time). This is a reasonable assumption considering that the timescale at which diffusion occurs is much smaller than that of the phenomena studied here. Therefore transitional states will not have considerable impact on the global outcome and can be deemed negligible. It should also be noted that NEURON resolves model equations in a one-dimensional manner, hence 1D diffusion is assumed.

Given these assumptions the diffusion flux between two adjacent compartments can be derived as:

$$J_{ion} = D_{ion} \frac{([\phi_{ion}]_{n+1} - [\phi_{ion}]_n)}{d_{n,n+1}} \quad (\text{A.17})$$

where  $J_{ion}$  is the molar flux for an  $ion$  species,  $D_{ion}$  is the longitudinal diffusion coefficient,  $[\phi_{ion}]_n$  is the  $ion$  concentration of the  $n^{\text{th}}$  compartment, and  $d_{n,n+1}$  is the distance between the two internal nodes of the adjacent compartment. The change in ion concentration resulting from the different ionic currents passing through the membrane can then be calculated by:

$$\frac{d[\phi_{ion}]_n}{dt} = i_{ion}(t) \frac{S}{V \cdot F} \quad (\text{A.18})$$

where  $i_{ion}(t)$  is the current for an  $ion$  species ( $\text{mA/cm}^2$ ),  $S$  is the total surface area,  $V$  is the compartmental volume, and  $F$  is the Faraday constant.

Contradictory to the H-H model, which is built to function at lower temperatures (default of 6.3 °C), the C-fibre model was developed for use at body temperature (37 °C). To achieve this the temperature coefficient, Q<sub>10</sub>, was set at 2.5 for voltage-dependent sodium channels and 3.3 for the potassium channels.

## C.2 Equations for Ionic Currents – Taken from Tigerholm et al (2014)

### *Na<sub>V</sub>I.7 current.*

$$\begin{aligned} I_{\text{Nav1.7}} &= g_{\text{Nav1.7}} \cdot m^3 h s \cdot (V_m - E_{\text{Na}}) \\ m &= m + [1 - \exp(-dt/\tau_m)] \cdot (m_{\text{inf}} - m) \\ \alpha_m &= 15.5 / \{1 + \exp[(V_m - 5) / (-12.08)]\} \\ \beta_m &= 35.2 / \{1 + \exp[(V_m + 72.7) / 16.7]\} \\ \tau_m &= 1 / (\alpha_m + \beta_m) * Q10_{\text{Na}} \\ m_{\text{inf}} &= \alpha_m / (\alpha_m + \beta_m) \\ h &= h + [1 - \exp(-dt/\tau_h)] \cdot (h_{\text{inf}} - h) \\ \alpha_h &= 0.38685 / \{1 + \exp[(V_m + 122.35) / 15.29]\} \\ \beta_h &= -0.00283 + 2.00283 / \{1 + \exp[(V_m + 5.5266) / (-12.70195)]\} \\ \tau_h &= 1 / (\alpha_h + \beta_h) * Q10_{\text{Na}} \\ h_{\text{inf}} &= \alpha_h / (\alpha_h + \beta_h) \\ s &= s + [1 - \exp(-dt/\tau_s)] \cdot (s_{\text{inf}} - s) \\ \alpha_s &= 0.00003 + 0.00092 / \{1 + \exp[(V_m + 93.9) / 16.6]\} \\ \beta_s &= 132.05 - 132.05 / \{1 + \exp[(V_m + 384.9) / 28.5]\} \\ \tau_s &= 1 / (\alpha_s + \beta_s) * Q10_{\text{Na}} \\ s_{\text{inf}} &= \alpha_s / (\alpha_s + \beta_s) \end{aligned}$$

### *Na<sub>V</sub>I.8 current.*

$$\begin{aligned} I_{\text{Nav1.8}} &= g_{\text{Nav1.8}} \cdot m^3 h s u \cdot (V_m - E_{\text{Na}}) \\ m &= m + [1 - \exp(-dt/\tau_m)] \cdot (m_{\text{inf}} - m) \\ \alpha_m &= 2.85 - 2.839 / \{1 + \exp[(V_m - 1.159) / 13.95]\} \\ \beta_m &= 7.6205 / \{1 + \exp[(V_m + 46.463) / 8.8289]\} \\ \tau_m &= 1 / (\alpha_m + \beta_m) * Q10_{\text{Na}} \\ m_{\text{inf}} &= \alpha_m / (\alpha_m + \beta_m) \\ h &= h + [1 - \exp(-dt/\tau_h)] \cdot (h_{\text{inf}} - h) \\ \tau_h &= 1.218 + 42.043 \cdot \exp\{-[(V_m + 38.1)^2 / (2 \cdot 15.19^2)]\} * Q10_{\text{Na}} \\ h_{\text{inf}} &= 1 / \{1 + \exp[(V_m + 32.2) / 4]\} \\ ds/dt &= (s_{\text{inf}} - s) / \tau_s \\ s_{\text{inf}} &= 1 / \{1 + \exp[(V_m + 45) / 8]\} \\ \tau_s &= 1 / (\alpha_s + \beta_s) * Q10_{\text{Na}} \\ \alpha_s &= 0.001 \cdot 5.4203 / \{1 + \exp[(V_m + 79.816) / 16.269]\} \\ \beta_s &= 0.001 \cdot 5.0757 / \{1 + \exp[-(V_m + 15.968) / 11.542]\} \\ du/dt &= (u_{\text{inf}} - u) / \tau_u \\ u_{\text{inf}} &= 1 / \{1 + \exp[(V_m + 51) / 8]\} \\ \tau_u &= 1 / (\alpha_u + \beta_u) * Q10_{\text{Na}} \\ \alpha_u &= 0.0002 \cdot 2.0434 / \{1 + \exp[(V_m + 67.499) / 19.51]\} \\ \beta_u &= 0.0002 \cdot 1.9952 / \{1 + \exp[-(V_m + 30.963) / 14.792]\} \end{aligned}$$

### *Na<sub>V</sub>I.9 current.*

$$\begin{aligned} I_{\text{Nav1.9}} &= g_{\text{Nav1.9}} \cdot m h s \cdot (V_m - E_{\text{Na}}) \\ \alpha_m &= 1.032 / \{1 - \exp[(V_m + 6.99) / 14.87115]\} \\ \beta_m &= 5.79 / \{1 + \exp[(V_m + 130.4) / 22.9]\} \\ \alpha_h &= 0.06435 / \{1 + \exp[(V_m + 73.26415) / 3.71928]\} \\ \beta_h &= 0.13496 / \{1 + \exp[(V_m + 10.27853) / (29.09334)]\} \\ \alpha_s &= 0.00000016 \cdot \exp(-V_m / 12) \\ \beta_s &= 0.0005 / \{1 + \exp[-(V_m + 32) / 23]\} \\ m_{\text{inf}} &= \alpha_m / (\alpha_m + \beta_m) \\ \tau_m &= 1 / (\alpha_m + \beta_m) * Q10_{\text{Na}} \\ h_{\text{inf}} &= \alpha_h / (\alpha_h + \beta_h) \\ \tau_h &= 1 / (\alpha_h + \beta_h) * Q10_{\text{Na}} \\ s_{\text{inf}} &= \alpha_s / (\alpha_s + \beta_s) \end{aligned}$$

### *K<sub>dr</sub> current.*

$$\begin{aligned} I_{\text{Kdr}} &= g_{\text{Kdr}} \cdot n^4 \cdot (V_m - E_K) \\ dn/dt &= (n_{\text{inf}} - n) / \tau_n \\ n_{\text{inf}} &= 1 / \{1 + \exp[-(V_m + 45) / 15.4]\} \\ \tau_n &= 1,000 \cdot (0.000688 + 1 / \{\exp[(V_m + 75.2) / 6.5] \\ &\quad + \exp[(V_m - 131.5) / -34.8]\}) * Q10_K, \text{ if } V_m \leq 31 \text{ mV} \\ \tau_n &= 0.16 + 0.8 \cdot \exp[-0.0267 \cdot (V_m + 11)] * Q10_K, \text{ if } V_m > -31 \text{ mV} \end{aligned}$$

### *K<sub>M</sub> current.*

$$\begin{aligned} I_{\text{KM}} &= g_{\text{KM}} \cdot (n_s / 4 + 3n_f / 4) \cdot (V_m - E_K) \\ dn_s/dt &= (n_{\text{inf}} - n) / \tau_{ns} \\ dn_f/dt &= (n_{\text{inf}} - n) / \tau_{nf} \\ n_{\text{inf}} &= 1 / \{1 + \exp[-(V_m + 30) / 6]\} \\ \text{if } (V_m < -60) \{ \tau_{ns} = 219 * Q10_K \}, \text{ else} & \tau_{ns} = 13 \cdot V_m + 1,000 * Q10_K \\ \tau_{nf} &= 1 / (\alpha + \beta), \text{ with } \alpha = 0.00395 \cdot \exp[(V_m + 30) / 40] \\ & \text{and } \beta = 0.00395 \cdot \exp[-(V_m + 30) / 20] * Q10_K \end{aligned}$$

### *K<sub>A</sub> current.*

$$\begin{aligned} I_{\text{KA}} &= g_{\text{KA}} \cdot nh \cdot (V_m - E_K) \\ dn/dt &= (n_{\text{inf}} - n) / \tau_n \\ dh/dt &= (h_{\text{inf}} - h) / \tau_h \\ n_{\text{inf}} &= (1 / \{1 + \exp[-(V_m + 5.4 + 15) / 16.4]\})^4 \\ \tau_n &= 0.25 + 10.04 \cdot \exp\{-[(V_m + 24.67)^2 / (2 \cdot 34.8^2)]\} * Q10_K \\ h_{\text{inf}} &= 1 / \{1 + \exp[(V_m + 49.9 + 15) / 4.6]\} \\ \tau_h &= 20 + 50 \cdot \exp\{-(V_m + 40)^2 / (2 \cdot 40^2)\} * Q10_K \\ & \text{if } \tau_h < 5 \text{ then } \tau_h = 5 \end{aligned}$$

*h* current.

$$I_{h,Na} = 0.5 \cdot g_h \cdot (0.5n_s + 0.5n_f) \cdot (V_m + E_{Na})$$

$$I_{h,K} = 0.5 \cdot g_h \cdot (0.5n_s + 0.5n_f) \cdot (V_m + E_K)$$

$$n_s = 1 / \{1 + \exp[(V_m + 87.2)/9.7]\}$$

$$n_f = 1 / \{1 + \exp[(V_m + 87.2)/9.7]\}$$

$$dn_s/dt = (n_{inf,s} - n_s)/\tau_{n,s}$$

$$dn_f/dt = (n_{inf,f} - n_f)/\tau_{n,f}$$

$$\tau_{n,s} = 300 + 542 \cdot \exp[(V_m + 25)/20] * Q10_H \text{ if } V_m > -70$$

$$\tau_{n,s} = 2,500 + 100 \cdot \exp[(V_m + 240)/50] * Q10_H \text{ if } V_m < -70$$

$$\tau_{n,f} = 140 + 50 \cdot \exp[(V_m + 25)/-20] * Q10_H \text{ if } V_m > -70$$

$$\tau_{n,f} = 250 + 12 \cdot \exp[(V_m + 240)/50] * Q10_H \text{ if } V_m < -70$$

*K<sub>Na</sub>* current.

$$I_{KNa} = g_{KNa} \cdot w \cdot (V_m - E_K)$$

$$w = 1 / [1 + (38.7/Na_{in})^{3.5}]$$

Leak currents.

$$I_{leak} = g_{Kleak} \cdot (V_m - E_K) + g_{Na leak} \cdot (V_m - E_{Na})$$

$$g_{Na leak} = -(ina_{Nav1.7} + ina_{Nav1.9} + ina_{Nav1.8} + ina_h + ina_{NaKpump}) / (V_{rest} - E_{Na})$$

$$g_{Kleak} = -(ik_{KM} + ik_{KA} + ik_h + ik_{Kdr} + ik_{NaKpump} + ik_{KNa}) / (V_{rest} - E_K)$$

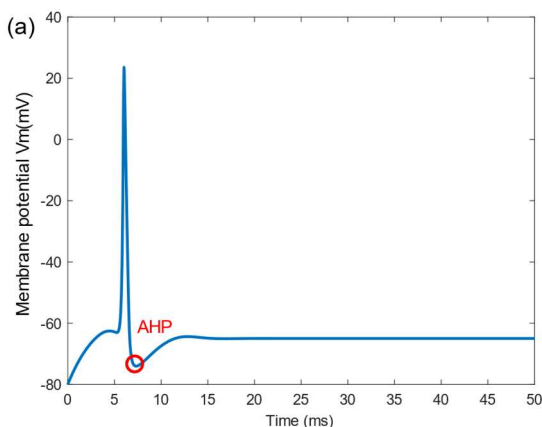
Na-K-ATPase currents.

$$I_{K,pump} = g_{pump} / [(1 + 1/K_{sp})^2] \cdot (1.62 / \{1 + [6.7/(Na_{in} + 8)]^3\} + 1.0 / \{1 + [67.6/(Na_{in} + 8)]^3\})$$

$$I_{Na,pump} = -3/2 \cdot I_{K,pump}$$

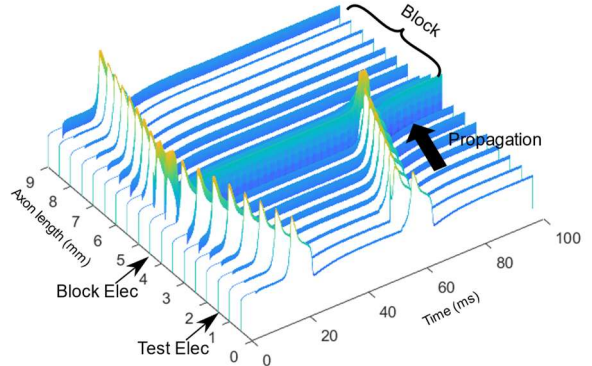
$$I_{pump} = I_{K,pump} + I_{Na,pump}$$

### C.3 C-fibre/H-H model comparison and validation



### C.2 Demonstration of block – C-fibre model

(a) Block, 10kHz, 102mA



(a) No block, 10kHz, 101mA

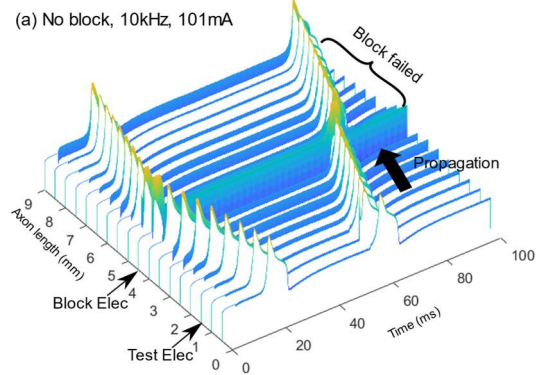
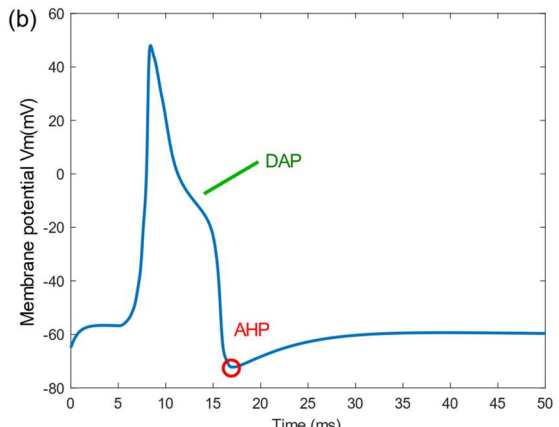


Figure A-6: (Top) Demonstration of block in C-fibre model at stimulation frequency of 10kHz and intensity of 102mA. (Bottom) Failure to achieve block at same frequency and intensity of 101mA.



*Figure A-7: A comparison of the AP waveforms produced by the H-H model and the C-fibre model. (a) H-H model (b) C-fibre model. The C-fibre model produces a much wider spike and a noticeably large depolarising after potential (DAP) lasting approximately 3-4ms which is not apparent in the H-H AP. Spikes from both models are followed by a hyperpolarising after potential (AHP) before settling back to resting potential. The AP shape of the C-fibre model produced here is fairly consistent with that shown in Tigerholms et al's works [28], [29], however the AHP is more pronounced in this present study. It should be noted that the details regarding the relative influence of the underlying currents on the shape of AP waveforms in C-fibre axons are currently unknown according to the literature [28].*

*One major difference between the H-H model and the C-fibre model is the reduction in conduction velocity across all diameters investigated as shown in Table 3-1. Furthermore, in comparison to Tigerholms et al's works [28] conduction velocity was much lower in the present study for a C-fibre axon of the same diameter (for 1 $\mu$ m axon, present study: 0.18m/s, Tigerholm: 0.69m/s). According to Obreja et al (2010) [35], C-fibre conduction velocity should lie between 0.6 and 1.3m/s, meaning none of the different diameters of C-fibre investigated in this present study met that condition despite being larger in diameter than the recorded physiological norm (<1 $\mu$ m)[35], suggesting you would see an increase in conduction velocity.*

#### C.4 Supression of onset response - 1 $\mu$ m C-fibre model

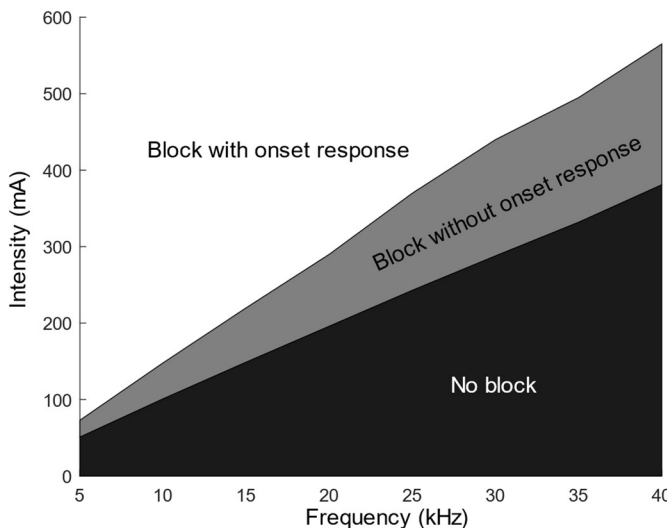
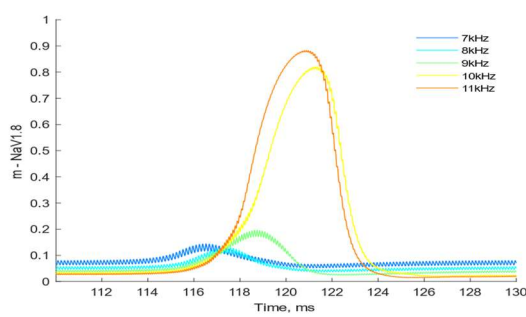


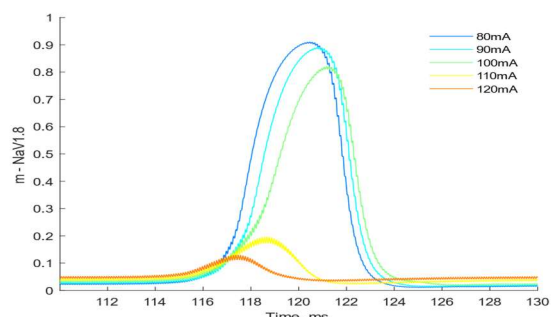
*Figure A-8: Suppression of onset response in 1 $\mu$ m C-fibre axon model. IED: 1mm. Black – No block, Grey – Block without onset response, White – Block with onset response. As frequency increases the range of intensities in which block can be achieved without onset response increases.*

#### C.5 C-fibre gating variables of the central node for experiments with fixed frequency and fixed intensity.

(a)



(d)



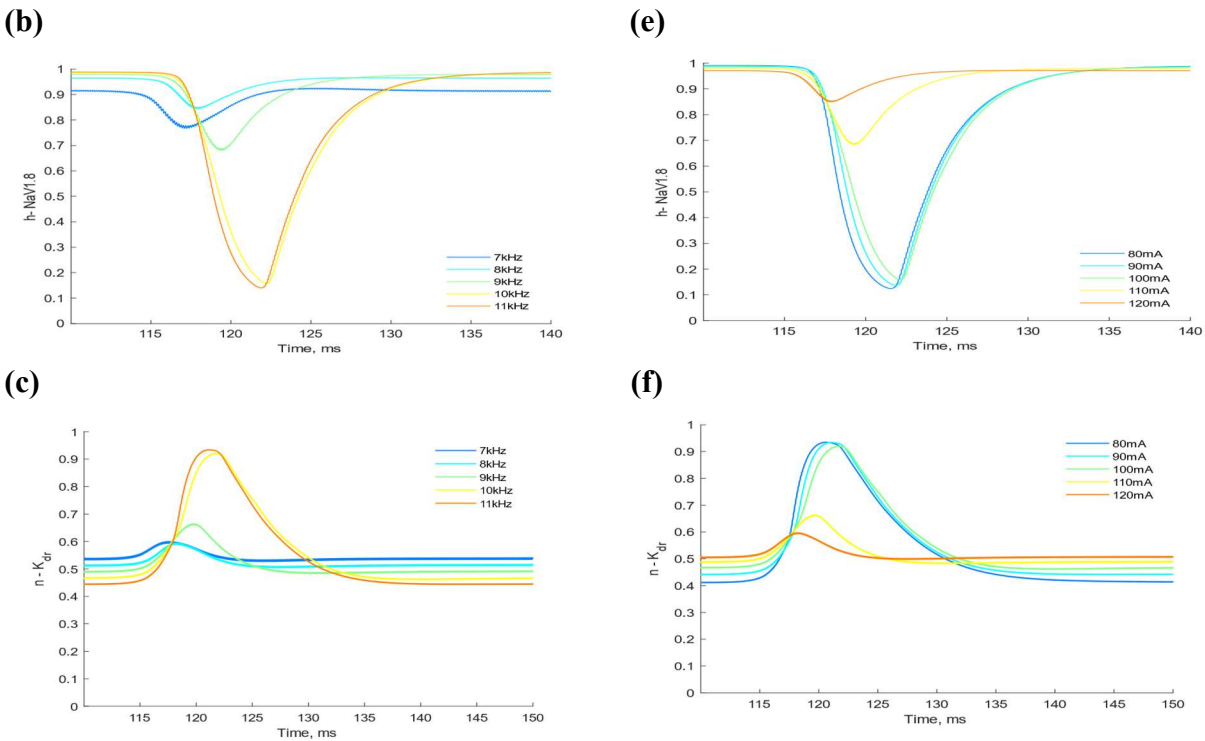


*Figure A-8: (a-c) ion channel gating variables for the segment/compartment under the block electrode (node 18) over 5 frequencies; 7,8,9,10,11kHz, and a fixed amplitude of 100mA during the time of block. (a) NaV1.8 activation, m (b) NaV1.8 inactivation, h (c) potassium delayed-rectifier activation, n. Frequencies of 7,8 and 9kHz achieved conduction block whereas 10 and 11kHz both failed. For the NaV1.8 activation variable a lower frequency results in a slightly higher activation at steady state (a), but still for all frequencies remains almost closed (0-0.1). The inactivation variable inversely maintains a slightly decreased value with lower frequency at steady state (b). Finally, the potassium delayed-rectifier activation variable maintains a higher activation level (c) at a lower frequency at steady state. In the same manner as the H-H model conduction block occurs when the activation of potassium during steady state is just above a threshold of roughly 0.48. This compares to a threshold of 0.45 for the H-H model which may explain the slightly increased block threshold curves of the C-fibre model shown in Figure 3-2.*

*(d-f) the same variables are shown at the time of block for five different intensities of stimulation; 80, 90, 100, 110, 120mA, and a fixed frequency of 10kHz. Block was achieved for intensities of 110 and 120mA. Results show an inverse of those in **Error! Reference source not found.**(a-c), with the same potassium activation threshold of roughly 0.48 found.*